Proceedings of the 13th Asian Congress of Fluid Mechanics
17-21 December 2010, Dhaka, Bangladesh

Vorticity Dynamics in Complex Flow Diagnosis and Management

Jiezhi Wu[1*], Xiyun Lu[2], Yantao Yang[1] and Rikui Zhang[1]

[1] State Key Laboratory of Turbulence and Complex System, College of Engineering, Peking University, Beijing, 100871, China

[2] Department of Modern Mechanics, University of Science and Technology of China, Hefei, Anhui 230026, China

[*] E-mail of presenting author: jzwu@coe.pku.edu.cn

Abstract

The complexity of various Newtonian fluid flows encountered in nature and technology come from the coexistence of three nonlinear fundamental processes (or modes) and their couplings, both in the interior of the fluid and on boundaries: shearing process (vortex mode), compressing process (sound mode), and irreversible thermodynamic process (entropy mode). These processes are characterized by their respective localized but strong structures and interactions which can dominate the global flow performances. The more complex could such a flow be, the more desirable it is to decompose the flow into its most elementary building blocks, such that the key flow structures and interactions can be examined separately and understood clearly. A general theoretical framework for multiple-process splitting and coupling is being developed to this end. It permits identifying proper indicators for those key flow structures and interactions, and revealing how they act in global flow performances. Therefore, the theory provides a rational and powerful tool for engineering flow diagnosis and optimal configuration design/flow control. In this article we review this theory with emphasis on its physical background and demonstrate its applications to several practical complex flow diagnoses and management.

Keywords Multi-process decomposition and coupling, local dynamics theory, boundary vorticity flux, engineering flow diagnosis and management.

1 Introduction

The motion patterns of fluids of small viscosity, such as air and water in nature and technology, are amazingly rich and extremely complicated owing to big variety of flow structures. After Leonardo da Vinci's keen observation of vortical structures, Helmholtz [1] and Kelvin [2] laid down the theoretical basis for vortex motion. In the same seminal paper Helmholtz [1] also introduced the famous intrinsic decomposition of a vector field into a longitudinal (potential) part $\nabla\phi$ and a transverse (rotational) part $\nabla \times \boldsymbol{\psi}$, say, which foresaw two fundamental processes in a fluid motion: *compressing* and *shearing*, respectively (e.g. [3], [4]). References [5] and [6] then added the coupling of these fluid-dynamic processes with irreversible thermodynamic process measured by entropy increment. Since then it has been a consensus that the complexity of fluid motion, in particular with small viscosity μ or at large Reynolds numbers Re, has its origin at the coexistence and coupling of these three "modes" or processes, as exhibited by the characteristic structures and waves of each process, their nonlinear evolutions, instabilities, and interactions. These structures are highly localized and occupy only a very small portion of the flow domain, but may serve as organizers of the entire flow. They are measured by the *variation* of primitive flow variables $(\boldsymbol{u}, p)$ – velocity and pressure – rather than these variables themselves.

Owing to this conceptual development, in the study of complex flows it would be very beneficial to shift one's attention from global and smooth flow regions to those key localized structures, and from the original Navier-Stokes (NS) equations as a whole to their intrinsically split constituents for each fundamental process and its coupling with the others. These topics fall into a general theory of *multiple-process decomposition and coupling*. It is not only of fundamental interest but also of great engineering value. Every complex engineering flow has a set of global performances as its design objectives, e.g., the lift/drag ratio of a wing, the moment of a rotor blade, and the efficiency of a turbine, etc. These performances are determined by some key flow structures and their stability. The task of complex flow diagnosis is to pinpoint those key local structures and identify their physical origin. The ultimate goal of diagnosis is to improve the performance by effective flow management, including optimal configuration design and/or efficient flow control. In both diagnosis and management the theory of process decomposition and coupling may serve as a powerful and quantitative tool.

Within this theoretical framework, the most matured and widely applied branch is the *vorticity and vortex dynamics*, which we define as the theory on the shearing process measured by the vorticity and its coupling with

compressing and thermal processes [7]. Accordingly, the present article about complex vortical flow diagnosis and management is focused on a subfield of this branch. The main issues to be dealt with in the article are:

— An outline of the basic ideas of process decomposition and coupling both in the interior of a vortical flow and on the flow boundary (§ 2);

— Identification of the most important local indicators of vortical flow structures and interactions inside the flow field, and those on-boundary physical roots of these structures (§ 3). In flow diagnosis these indicators are the local quantities one should survey with high priority;

— Construction of integral expressions for global flow performances, in which the integrands are explicitly those identified key indicators of local structures and interactions (§ 4). While our presentation is focused on the total force and moment, other performances can be treated in a similar way;

— Examples of applying the theoretical results from vorticity and vortex dynamics to complex flow diagnosis and management (§ 5), followed by brief concluding remarks (§ 6).

2 Fundamental Processes and Their Coupling

The *Helmholtz decomposition* of a vector field mentioned in § 1 is a rational tool to *dynamically* decompose the NS equations into respective governing equations for shearing and compressing processes and to identify their coupling mechanisms. In this section we briefly outline the results obtained so far.

Let $\boldsymbol{a} = D\boldsymbol{u}/Dt$ be the fluid acceleration, $\boldsymbol{\omega} = \nabla \times \boldsymbol{u}$ and $\vartheta = \nabla \cdot \boldsymbol{u}$ the vorticity and dilatation, respectively, ρ the density, μ the shear viscosity (assumed constant for simplicity), $\mu_\theta = \zeta + 4\mu/3$ the longitudinal viscosity (ζ is the bulk viscosity), and $\Pi = p - \mu_\theta \vartheta$ the normal stress consisting of the pressure p and a viscous-dilatation term. Truesdell [8] points out that the body force (inertial force $-\rho\boldsymbol{a}$ plus external force $\rho\boldsymbol{f}$) per unit volume has a natural Helmholtz decomposition, since the NS equation can be written as

$$\rho(-\boldsymbol{a} + \boldsymbol{f}) = \nabla\Pi + \nabla \times (\mu\boldsymbol{\omega}), \tag{1}$$

of which the two terms on the right-hand side represent the compressing and shearing processes, respectively. Each of these processes plays dominant role in a flow field through very different flow structures. The most important compressing structure is shock wave associated to large (negative) peak of ϑ. In contrast, the shearing structures are characterized by large concentrated $\boldsymbol{\omega}$, such as boundary layers, free shear layers and axial vortices.

Each of the fundamental processes evolves nonlinearly, and meanwhile they interact with each other both inside the flow field and on the boundary. The most active nonlinearity and coupling are caused by the inherent nonlinearity of the acceleration $\boldsymbol{a}$, which itself should be decomposed. We thus turn to the NS equation per unit mass, considering the Crocco-Vazsonyi equation with constant dynamic viscosities, in which the vorticity $\boldsymbol{\omega}$ and entropy gradient ∇s appear maximally:

$$\boldsymbol{u}_{,t} + \boldsymbol{\omega} \times \boldsymbol{u} = -\nabla H + T\nabla s + \nu_\theta \nabla\vartheta - \nu\nabla \times \boldsymbol{\omega}, \tag{2}$$

whereafter the suffix $,t$ denotes partial derivative with respect to time; $H = h + |\boldsymbol{u}|^2/2$ is the total enthalpy with h being the enthalpy, T the temperature; and ν and ν_θ are the kinematic counterpart of μ and μ_θ, which are assumed nearly constant for neatness. We also dropped the body force $\boldsymbol{f}$. Then the curl and divergence of (2) yield [7]

$$\boldsymbol{\omega}_{,t} - \nu\nabla^2\boldsymbol{\omega} = -\nabla \times (\boldsymbol{\omega} \times \boldsymbol{u} - T\nabla s), \tag{3a}$$

$$\vartheta_{,t} - \nu_\theta\nabla^2\vartheta + \nabla^2 H = -\nabla \cdot (\boldsymbol{\omega} \times \boldsymbol{u} - T\nabla s). \tag{3b}$$

It is well known that the vorticity transport equation (3a) governs the shearing process. In contrast, the dilatation transport equation (3b) alone is insufficient for describing the compressing processes; it has to be combined with the continuity equation, which makes the general formulation for compressing more involved. For a new approach see [9] and [10].

The only common quantity $\boldsymbol{\omega} \times \boldsymbol{u} - T\nabla s$ in both (3a) and (3b) represents a nonlinear and inviscid coupling between the two processes inside the flow field, dominated by the Lamb vector $\boldsymbol{l} \equiv \boldsymbol{\omega} \times \boldsymbol{u}$. This vector is more localized and contains more information than the vorticity field because it reflects the interaction between the vorticity and neighboring velocity field. While (3a) indicates that $\nabla \times \boldsymbol{l}$ affects the shearing process by causing the advection, tilting, and stretching of vorticity lines, (3b) suggests that $\nabla \cdot \boldsymbol{l}$ is a source of sound [11]. This brief observation already suffices to indicate that the Lamb vector and its curl and divergence deserve a further examination. This will be done in § 3.

In contrast to the decomposed but coupled equations (3) for shearing and compressing processes, applying (1) on a no-slip wall, we obtain a pair of viscous and apparently linear normal-tangential $(\boldsymbol{\omega}, \Pi)$ coupling relations:

$$-\frac{1}{\rho}\frac{\partial\Pi}{\partial n} = \boldsymbol{n} \cdot (\boldsymbol{a}_B - \boldsymbol{f}) + \nu(\boldsymbol{n} \times \nabla) \cdot \boldsymbol{\omega}, \tag{4a}$$

$$\nu\frac{\partial\boldsymbol{\omega}}{\partial n} = \boldsymbol{n} \times \left(\boldsymbol{a}_B - \boldsymbol{f} + \frac{1}{\rho}\nabla\Pi\right) + \nu(\boldsymbol{n} \times \nabla) \times \boldsymbol{\omega}. \tag{4b}$$

The coupling with entropy process can be made explicitly by replacing $\nabla p/\rho$ in (4) by $\nabla h - T\nabla s$.

The operator $\boldsymbol{n} \times \nabla$ in (4) is of $\mathcal{O}(1)$. Thus, for flows with $Re \gg 1$, at the right-hand sides of both (4a) and (4b) the viscous terms are small compared to others. Namely, the normal gradient of Π is mainly produced by the wall-normal acceleration and body force, while the normal gradient of the vorticity is dominated by the tangential components of the wall acceleration, body force, and in particular the tangential gradient of Π. This latter balance is of crucial importance in flow diagnosis and management, because its left-hand side defines the *boundary vorticity flux* (BVF) $\boldsymbol{\sigma} \equiv \nu \partial \boldsymbol{\omega}/\partial n$ that, as identified by Lighthill [12], is the rate at which the vorticity is created at the wall by the no-slip condition and sent into the flow by diffusion.

Take incompressible flow as example, (4b) reveals that BVF has four origins:

$$\boldsymbol{\sigma} = \boldsymbol{\sigma}_a + \boldsymbol{\sigma}_p + \boldsymbol{\sigma}_f + \boldsymbol{\sigma}_v \tag{5a}$$

where

$$\begin{array}{ll} \boldsymbol{\sigma}_a = \boldsymbol{n} \times \boldsymbol{a}_B, & \boldsymbol{\sigma}_p = \frac{1}{\rho} \boldsymbol{n} \times \nabla p, \\ \boldsymbol{\sigma}_f = -\boldsymbol{n} \times \boldsymbol{f}, & \boldsymbol{\sigma}_v = \nu(\boldsymbol{n} \times \nabla) \times \boldsymbol{\omega}. \end{array} \tag{5b}$$

Here, $\boldsymbol{\sigma}_v$ is usually small as just mentioned. $\boldsymbol{\sigma}_a$ is important for flows with moving or deforming boundaries such as animal locomotion. It is also important for flow controls with flexible walls, such as turbulent drag reduction by spanwise traveling tangential wave [13] and bluff-body wake elimination by streamwise traveling normal waves [14]. $\boldsymbol{\sigma}_f$ plays a similar role in flow control as $\boldsymbol{\sigma}_a$ does, such as turbulent drag reduction by traveling wave of the Lorentz force in electronically conducting fluid [15],[16], as explained by [13]. While these mechanisms may sometimes be absent, $\boldsymbol{\sigma}_p$ is always there; for flow over a stationary wall without body force, we simply have

$$\boldsymbol{\sigma} \simeq \boldsymbol{\sigma}_p \equiv \frac{1}{\rho} \boldsymbol{n} \times \nabla p, \tag{6}$$

which is of $\mathcal{O}(1)$ at any Re. This key BVF constituent will be further examined in § 3.

3 Key Indicators for Vortical Structures and Interactions

Having obtained the process decomposition and coupling equations both in the interior of the flow and at boundary, our next task is to identify the key local indicators of vortical structures and interactions to be examined with high priority in complex flow diagnosis. We have seen in § 2 that the Lamb vector $\boldsymbol{l} \equiv \boldsymbol{\omega} \times \boldsymbol{u}$ and the pressure-caused BVF $\boldsymbol{\sigma}_p$ stand at the crossroad of shearing and compressing processes in the interior and on the boundary of the flow, respectively. In addition to process coupling, the Lamb vector is also the unique mechanism in (3a) responsible for the self-nonlinearity in vortex motion.[1] Therefore, the various aspects of $\boldsymbol{l}$ and $\boldsymbol{\sigma}_p$ relevant to local flow diagnosis and global (integrated) flow performance are naturally our main concern, and will be explored in this and the next sections, respectively.

If a fresh observer walks into an incompressible vortical flow at a large Reynolds number, he or she would first see the strongest vortical structures — *axial vortices*; only after a more careful examination the observer would find viscous free shear layers whose rolling up forms the axial vortices, and then boundary layers that form the free layers by separation. These *sheet-like vortices* are the primitive but weaker vortical structures. Their origin could then be traced to the vorticity creation at solid boundaries. This order by which the observer would learn vorticity and vortex dynamics will be followed in our presentations in this and the next sections. It is also a natural order for conducting complex flow diagnosis and management to be exemplified in § 5: typically, one first identifies the most favorable and unfavorable strong structures inside the flow field, then traces their causes to near-wall flow, and finally performs optimal design or flow control by managing their on-wall root.

3.1 Lamb Vector as the Vortex Force

In the Crocco-Vazsonyi equation (2), the Lamb vector of a fluid element represents a *lateral* acceleration perpendicular to both directions of velocity and vorticity. Thus $\boldsymbol{u} \times \boldsymbol{\omega}$ is an inertial force acting on the fluid element (i.e., a local rate of change of momentum per unit mass), known as the *vortex force*. This idea was originated in [17] and was extensively used in [18]-[20], among others. Its characteristic structure immediately reminds us that the vortex force must be the very origin and localized form of the famous Kutta-Joukowski formula, and hence plays a central role in vortical interactions. While this assertion will be conformed in § 4 when we consider integrated performances, here we explore the implication of the Lamb vector as a local force.

For simplicity we work within the vortex-sheet dynamics, which considers the asymptotic behavior of shear layers of thickness $\delta \to 0$ as $Re \to \infty$. Assume

[1] Strictly, the Lamb vector also contains coupling with the compressing process, because the velocity $\boldsymbol{u}$ may come from both processes.

that at both sides of the vortex sheet the flows have potential ϕ and come from the same upstream fluid. Then the sheet moves at the averaged velocity $\overline{\boldsymbol{u}}$ of both sides of the sheet, and we can introduce a circulation along a circuit across the sheet once, $\Gamma(\boldsymbol{x},t) = -[\![\phi]\!]$ that satisfies $D\Gamma/Dt = 0$,[2] in agreement with the Kelvin circulation theorem. Let $[\![f]\!] = f_1 - f_2$ be the jump of any variable f across the sheet and $\boldsymbol{n}$ be the normal pointing from side 2 to side 1, for the vortex sheet strength and its relation with Γ we have

$$\boldsymbol{\gamma} = \lim_{\delta\to 0}\int_0^\delta \boldsymbol{\omega} dn = \boldsymbol{n}\times[\![\boldsymbol{u}]\!] = -\boldsymbol{n}\times\nabla\Gamma. \tag{7}$$

The vortex-sheet Lamb vector is $\boldsymbol{\gamma}\times\overline{\boldsymbol{u}}$. A free vortex sheet does not stand any pressure jump; but the "bound vortex sheet" does, which represents a wing of negligible thickness enveloped by boundary layers. Correspondingly, the vortex force $\overline{\boldsymbol{u}}\times\boldsymbol{\gamma}$ has a two-fold implication: it is either a true lateral force if it is associated with a bound vortex sheet, or an inertial force if associated with a free vortex sheet. To illustrate this, consider two-dimensional incompressible flow on the (x,y)-plane and introduce an intrinsic curvilinear orthonormal frame $(\boldsymbol{t},\boldsymbol{n})$ along the sheet, with $\boldsymbol{t}\times\boldsymbol{n} = \boldsymbol{e}_z$, $\boldsymbol{u} = (u_s, u_n)$, and $\boldsymbol{\gamma} = \boldsymbol{e}_z\gamma$, so that

$$\gamma = \frac{\partial\Gamma}{\partial s},\quad \Gamma(s) = \int_{s_0}^{s}\gamma ds = \lim_{\delta\to 0}\int_0^\delta\int_{s_0}^{s}\omega ds dn, \tag{8}$$

where s_0 is an end point of the vortex sheet. Then from the Bernoulli equation we have the following dynamic equation [7], which highlights the dual role of not only the Lamb vector but also the time-variation of Γ:

$$\rho\frac{D\Gamma}{Dt} = \rho(\Gamma_{,t} + \gamma\overline{u}_s) = \begin{cases} [\![p]\!] & \text{for bound sheet,}\\ 0 & \text{for free sheet.}\end{cases} \tag{9}$$

In particular, for steady flow the pressure jump or the normal force acting to the bound vortex per unit length is balanced by the vortex force alone ([7],[18]):

$$[\![p]\!] = \rho\overline{u}_s\gamma. \tag{10}$$

This simple equation deserves a careful inspection. Firstly, it does not relate local quantities themselves but their jump or difference at two opposite local points, which is a degenerated version of certain variation of flow variables. As asserted in § 1, it is the variations of flow variables (e.g., the jump of tangential velocity) that can characterize structures (e.g., vortex sheet). Secondly, (10) offers a simple example that the variation of pressure, a compressing variable, can be replaced by some kind of vorticity, a shearing variable. They can be mutually transformed, but only the latter is a localized quantity. These remarks will be fully recognized in the context of equation (23) to be discussed in the next section.

As we go to the three-dimensional world, $\boldsymbol{\omega}$ and $\boldsymbol{u}$ will vary not only in their magnitude but also in their relative angle (say β), as is evident from the triangle identity

$$|\boldsymbol{u}|^2|\boldsymbol{\omega}|^2 = |\boldsymbol{\omega}\cdot\boldsymbol{u}|^2 + |\boldsymbol{\omega}\times\boldsymbol{u}|^2. \tag{11}$$

Thus, for given $|\boldsymbol{u}|$ and $|\boldsymbol{\omega}|$, *among various appearances of the vortex force the one that has nearly two-dimensional or rotationally symmetric behavior is the strongest.* It will be weakened when β reduces from the value $\pi/2$ in two-dimensional flow. When the flow becomes Beltramian (i.e., $\boldsymbol{\omega}\|\boldsymbol{u}$) the vortex force vanishes. What appears and grows as β decreases is the *helicity density* $\boldsymbol{\omega}\cdot\boldsymbol{u}$. This quantity does not directly enter the force interaction; its spatial integral represents the topology of thin vortex loops. However, it is worth mentioning that the Beltramian flow and helicity density are closely relevant to the further intrinsic decomposition of a vectorial shearing process into two intrinsic components, in terms of the polarities of the flow, e.g. [21]. This polarity decomposition is also a subclass of the process splitting and coupling in complex flows.

3.2 Lamb Vector in the Formation of Axial Vortices

The Lamb vector or vortex force is not only a characteristic indicator of the lateral force on a body or bound vortex sheet, but also an indicator of the dynamic evolution of a free vortex sheet which is constrained by the second line of (9). Among various motions of a free vortex sheet, we choose to exemplify this role of the vortex force by the vortex-sheet roll up, because as said before this process generates axial vortices that has important influence on the global flow behavior. In two-dimensional flow the vortex-sheet roll-up is fully governed by an elegant nonlinear and singular integral-differential equation known as the Birkhoff-Rott equation [20][22]; but it is helpful to make a qualitative and intuitive observation based on (8) to (10), as well as the two-dimensional version of the transport equation for $\boldsymbol{\gamma}$ (Eq. (4.154a) of [7]). Namely, denoting the vortex force by $\boldsymbol{f} = \overline{\boldsymbol{u}}\times\boldsymbol{\gamma} = (f_s, f_n)$, we have

$$f_s = \gamma\overline{u}_n,\quad f_n = -\gamma\overline{u}_s, \tag{12a}$$

$$\frac{D}{Dt}\ln\gamma = \overline{u}_n\kappa - \frac{\partial\overline{u}_s}{\partial s}, \tag{12b}$$

where κ is the curvature of the sheet and $\overline{u}_n$ is nonzero only for unsteady flow. Note that f_n in (12a) just balances $[\![p]\!]/\rho$ in (10).

[2] The sign of Γ defined here is opposite to that in [7].

We revisit a classic vortex sheet roll-up problem, the formation of wing-tip vortices. In the wind-axis system (x, y, z) with $x = 0$ located at the trailing edge, let the incoming flow be $\boldsymbol{U} = U\boldsymbol{e}_x$ and y, z axes be along the wing span and vertically up, respectively. In Prandtl's lifting-line theory, the wing with minimum induced drag has elliptical load distribution $\Gamma(y) = 2W\sqrt{a^2 - y^2}$, where $W = U\alpha$ with $\alpha \ll 1$ being the angle of attack. Thus on the sectional $(0, y, z)$-plane the bound vortex sheet has strength distribution

$$\gamma(y) = \frac{2Wy}{\sqrt{a^2 - y^2}}. \tag{13}$$

As $y \to \pm a$, γ has a singularity of the $|a-y|^{-1/2}$-type, and so does the pressure jump due to (10). This effect leads to a finite circulation around wing-tips which induces an upward flow at $y < -a$ and $y > a$, and a leading-edge suction familiar in classic thin airfoil theory [20][22].

As usual, we approximate the x-wise evolution of a steady three-dimensional wake vortex sheet by the time evolution of an unsteady two-dimensional vortex sheet on sectional (y, z)-planes at locations of increasing $x \simeq Ut$. Referring to (12) and Fig. 1 for the right portion of the vortex sheet pattern, some rough estimates can then be made.[3] For example:

— Right after the sheet leaves the trailing edge, the leading-edge suction in (10) immediately causes the end point s_1 to gain $u_n > 0, \kappa > 0$, and hence to move up. Then the big γ of s_1 induces the neighboring points at $s < s_1$ to run around it to quickly form a spiral.

— The spiral entrains more and more portion of the vortex sheet into it with $\overline{u}_s > 0$ and $f_n < 0$. The entrained portion is stretched with $\partial\overline{u}_s/\partial s > 0$, while the normal motion of s_1 is slowed down.

— The whole spiral also induces $\overline{u}_s > 0$ and $\overline{u}_n < 0$ on the portion of the sheet at its lower-left side, where the sheet moves downward.

— As time goes on, the rolled part of the sheet has increasingly many turns, of which the core region consists of nearly concentric circles with the flow being axisymmetric. Thus both $\overline{u}_n$ and $\partial\overline{u}_s/\partial s$ vanish and γ approaches constant.

It should be stressed that for a vortex sheet to roll up from its end point, the end point must have big γ. If

[3]Since the rolling up is an unsteady motion of a material sheet but the vortex force represents the local rate of change of the sheet momentum, a complete dynamic discussion of the roll up has to combine $\boldsymbol{f}$ and $\Gamma_{,t}$ into a whole along the sheet, which is not attempted here. Instead, we use both the dynamic estimate based on vortex force and a more intuitive kinematic estimate based on vortex induction.

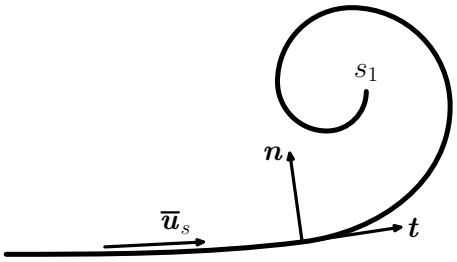

Figure 1: The rolling up of an initially straight vortex sheet.

$\gamma = 0$ there no this kind of roll up can happen. For example, the flat sheet on the x-axis between $x = \pm 1$ with strength $\gamma(x) = K\sqrt{1 - x^2}$ is an exact solution of the Birkhoff-Rott equation, which doe not roll up but makes rigid rotation [22]; it has $\gamma = 0$ at the end points. On the other hand, the leading points of roll up may also occurs somewhere away from the end points as long as the vortex force has proper initial behavior there. A typical example is a straight and infinitely extended vortex sheet disturbed by a sinusoidal wave (the Kelvin-Helmholtz instability), which leads to periodic double-branch roll up and hence forms an array of axial vortices.

Owing to the same mechanism of the Lamb-vector weakening in three-dimensional flows due to the reduction of the angle between $\boldsymbol{\omega}$ and $\boldsymbol{u}$, we may also say that *among all possible vortex-sheet rolling up patterns in a three-dimensional world, the one that has nearly two-dimensional or rotationally symmetric behavior is the strongest*, and when the flow becomes Beltramian the aforementioned entrainment of spiral vortex stops.

3.3 The Curl and Divergence of the Lamb Vector

Extensive discussions on the curl and divergence of the Lamb vector $\boldsymbol{l}$ have been made in [7]. Reference [23] further shows that $\nabla\cdot\boldsymbol{l}$ with opposite signs corresponds to very different local motion of the fluid: $\nabla\cdot\boldsymbol{l} > 0$ represents straining motions with local concentration of flow energy, while the regions with $\nabla \cdot \boldsymbol{l} < 0$ constitute the vortical motions with depleted flow energy. They found that the Lamb-vector divergence may also describe the interaction between the fluid with high- and low-momentum; in a turbulent channel flow $\nabla \cdot \boldsymbol{l}$ can well capture the "sweep" and "ejection" events which are highly relevant to the momentum exchange in the turbulent boundary layer.

Figure 2 exemplifies the distribution of $\nabla \cdot \boldsymbol{l}$ and $\nabla \times \boldsymbol{l}$ for a numerically computed compressible turbulent flow over an aerofoil [24]. Note that these patterns are very

different from those of $\boldsymbol{\omega}$ and ϑ for the same flow. The nearly streamwise strips of peak $\nabla \cdot \boldsymbol{l}$ in Figs. 2a and 2b are associated with the turbulent shear layers, where the strong momentum exchange occurs between the high- and low- speed fluids. The same regions are also captured by $\nabla \times \boldsymbol{l}$, indicating the rapid change of the vorticity due to the temporal evolution of the shear layer. Moreover, $\nabla \times \boldsymbol{l}$ is quite large in the shock wave regions, see the nearly vertical strips starting from the wing surface in Figs 2c and 2d, because the curve shock produces new vorticity; but these strips are not revealed by $\nabla \cdot \boldsymbol{l}$, indicating that although there is a very strong transition from high- to low-momentum across the shock wave the high/low-momentum interactions are weak.

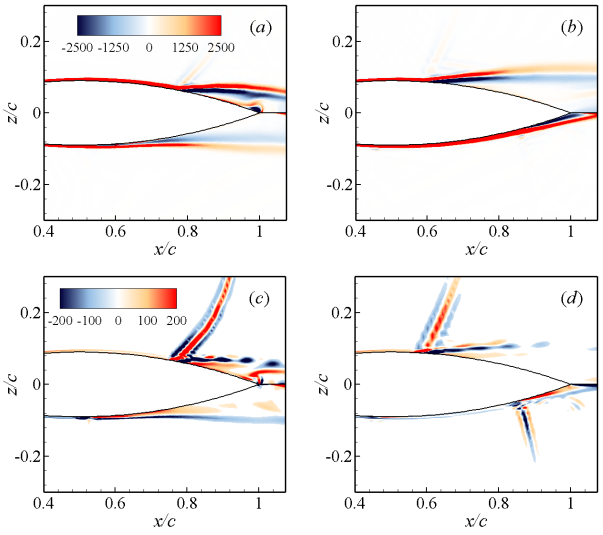

Figure 2: Instantaneous distributions of $\nabla \cdot \boldsymbol{l}$ at (a) $t^* = 0.5$ and (b) $t^* = 0.625$, and $\nabla \times \boldsymbol{l}$ at (c) $t^* = 0.5$ and (d) $t^* = 0.625$ [24]. t^* is dimensionless time.

3.4 Pressure-Caused Boundary Vorticity Flux

We now turn to the BVF caused by the pressure gradient, $\boldsymbol{\sigma}_p$. As stated by [25], the $\boldsymbol{\sigma}_p$ plays a dual role on the wall. On the one hand, as the tangential pressure gradient, $\boldsymbol{\sigma}_p$ is an on-wall signature of the entire flow and measures the local dynamics of compressing process. On the other hand, as a cause or on-wall root of the vorticity field, it measures the local dynamics of shearing process. For incompressible flow, the BVF is the only source of the vorticity in the entire flow field. It is a general rule that the evolution of boundary vorticity is a space-time accumulated effect of, and hence has a phase lag behind the BVF.

For example, in a two-dimensional attached boundary-layer on the (x, y)-plane, Fig. 3 (not to scale) sketches its velocity profile $u(y)$, vorticity profile $\omega(y) = -u'(y)$, and BVF $\sigma = -\nu\omega'(y)|_{y=0} = p'(x)$. The driving mechanism is clearly the pressure gradient $p'(x)$ in the potential flow outside the boundary layer. The newly generated $\omega > 0$ by a $\sigma_p > 0$, once diffused into the fluid, will weaken the existing $\omega < 0$ in the boundary layer. If this weakening mechanism continues to make ω change sign, flow separation will occur.

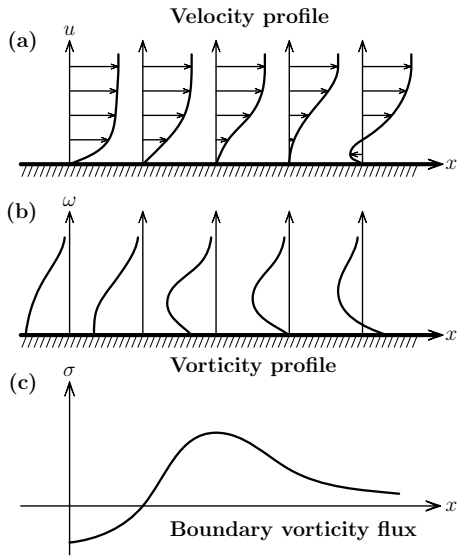

Figure 3: Sketch of the profiles of velocity (a), vorticity (b), and the variations of the fluxes of vorticity (c) on the wall, for a flat-plate flow in a pressure gradient changing from favorable to adverse. After [7].

This being the case, a BVF peak must signify some important local event in the boundary layer, including the whole boundary-layer separation that may alter the entire flow field. Indeed, according to the triple-deck theory, whenever there is some sudden change in downstream flow condition, for example a discontinuity of the wall slope or curvature, the flow in the sublayer adjacent to the wall has to adjust itself to fit the sudden change, which must cause an interaction with the outer potential flow associated with a local interactive pressure of $\mathcal{O}(Re^{-1/4}) \ll 1$. But this pressure increment occurs within a small interval of $\mathcal{O}(Re^{-3/8})$, resulting in a large local tangential pressure gradient and hence a BVF peak, of $\mathcal{O}(Re^{1/8}) \gg 1$. While the small interactive pressure is hard to capture by calculation or measurement, the big BVF peak can be easily found to make it a sensitive indicator of abrupt changes in the near-wall flow.

For instance, Fig. 4 compares the distributions of the pressure and BVF on the inducer surface of a centrifugal

pump. The former is quite smooth over the entire blade, but the latter has strong fluctuation at three streaks, which are precisely the locations known to easily have cracks. A subsequent study has confirmed that right at these streaks the surface curvature was discontinuous.

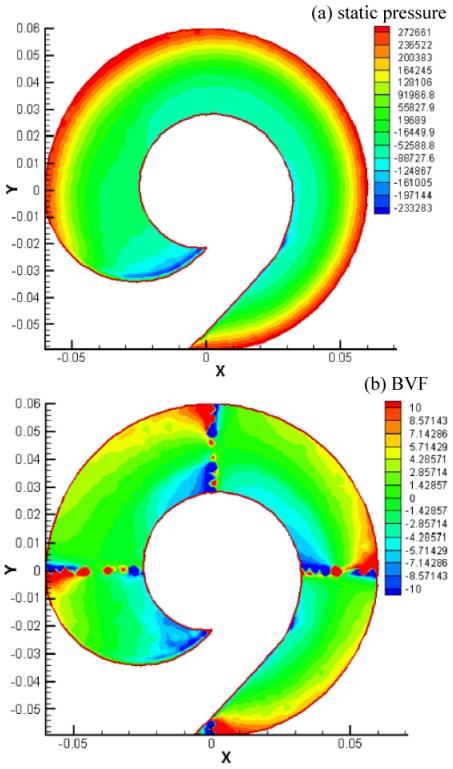

Figure 4: The distributions of the pressure (a) and BVF (b) on the inducer blade of a centrifugal pump [25].

In three-dimensional flow, like the relative orientation of $\boldsymbol{\omega}$ and $\boldsymbol{u}$ varies and matters, so does that of the on-wall vector lines of the skin-friction $\boldsymbol{\tau} = \mu\boldsymbol{\omega} \times \boldsymbol{n}$ and BVF in the analysis of near-wall flow patterns. While generically in smooth attached flow region the BVF lines have large angles with $\boldsymbol{\tau}$ lines as in two-dimensional flow, the big BVF peak in the narrow triple-deck zone may turn the BVF lines to the direction almost aligned to the $\boldsymbol{\tau}$ lines indicating that the boundary layer is separating. This is exemplified by Fig. 5 for the $(\boldsymbol{\sigma}_p,\ \boldsymbol{\tau})$-lines on the suction side of the rotor blade of a compressor. At the upper middle region, the red $\boldsymbol{\tau}$-lines converge and go upward, where the $\boldsymbol{\sigma}_p$-lines are basically along the same direction. Reference [12] proposed the convergence of the $\boldsymbol{\tau}$-lines to be the criterion of three-dimensional *flow separation*. But it is insufficient to characterize the *boundary-layer separation* unless the $(\boldsymbol{\sigma}_p,\ \boldsymbol{\tau})$ alignment is added.

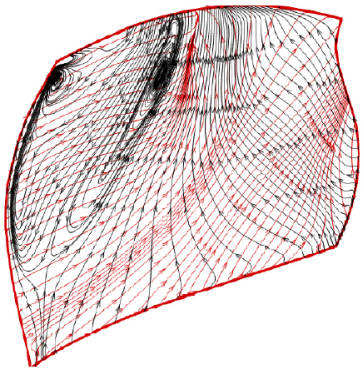

Figure 5: The vector lines of the skin-friction $\boldsymbol{\tau}_w$ (red) and BVF $\boldsymbol{\sigma}_p$ (black) on the suction side of a rotor blade of a transonic compressor [26].

3.5 The Formation of Near-Wall Lamb Vector

Having clarified the generation of vorticity at the wall, we may return to the Lamb vector $\boldsymbol{l}$ to look at its formation. Of course this must happen inside the boundary layer as well; and, above a stationary wall there must be a Lamb-vector maximum $\boldsymbol{l}_{\max}$ inside the boundary layer as illustrated in Fig. 6. Later we shall see that this $\boldsymbol{l}_{\max}$ is the major contributor of the entire vortex force acting on a wing. Here let us examine how this near-wall Lamb vector is formed and estimate its order of magnitude.

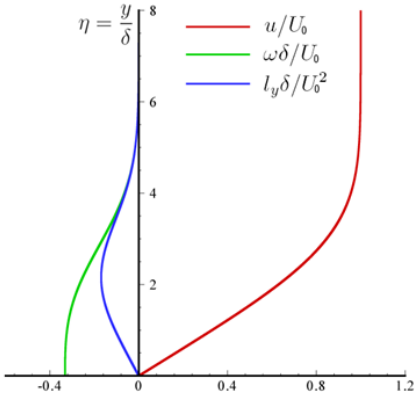

Figure 6: The normalized u, ω and $l_y = u\omega$ profiles in the Blasius boundary layer.

Let h be a small hight in an attached boundary layer. A Taylor expansion along the normal yields [27]

$$l_n = \omega_b^2 h - \frac{3}{2\nu}(\boldsymbol{\omega}_b \cdot \boldsymbol{\sigma})h^2 + O(h^3), \tag{14a}$$

$$\boldsymbol{l}_\pi = -\frac{1}{\nu}\sigma_n \boldsymbol{\omega}_b h^2 + O(h^3), \tag{14b}$$

where suffix π denotes tangential components of a vector, $\boldsymbol{\omega}_b$ is the on-wall vorticity, and σ_n is the normal component of the BVF. In general σ_n is an $O(Re^{-1/2})$ three-dimensional effect; it will be appreciable only in a small neighborhood of a spiral fixed point of the skin-friction field, associated with the formation of horn-like vortices. For the series to converge h should be at least as small as the boundary-layer thickness. Thus, in laminar flow the normal and tangential components of the Lamb vector, l_n and $|\boldsymbol{l}_\pi|$, are of $\mathcal{O}(Re^{1/2})$ and $\mathcal{O}(1)$, respectively. This implies that the wall-normal vortex force is dominant in these regions.

When the boundary layer separates the Taylor expansion does not work well. To illustrate the behavior of the Lamb vector in a zone surrounding the separation point s, we employ the triple-deck theory and consider two-dimensional steady separation. Let $(x,\ y)$ be the wall-parallel and wall-normal coordinates. Upstream the separation zone the boundary layer is attached and the above arguments are still true. Around a region with $x - x_s = O(Re^{-3/8})$, a viscous and rotational lower deck appears adjacent to the wall that introduces additional displacement and perturbation to the main and upper decks. The Lamb vector field is altered simultaneously.

In the upper potential-flow deck we still have $\boldsymbol{l} = \boldsymbol{0}$. The main deck is basically the upstream boundary layer lifted by the new lower deck, where the perturbed flow quantities are [7][28]

$$(u, v, \omega) = (U_B, \delta^4 V_B, \delta^{-4}\Omega_B) + (\delta\widetilde{U}, \delta^2\widetilde{V}, \delta^{-3}\widetilde{\Omega}) + \cdots,$$

where the capital letters denote the normalized quantities of $O(1)$, subscript B stands for quantities of the upstream attached boundary layer, and $\delta = O(Re^{-1/8}) \ll 1$ is a new length scale. Then we find

$$\begin{aligned} l_x &= -Re^{1/4}\Omega_B\widetilde{V} + O(Re^{1/8}), && \text{(15a)}\\ l_y &= Re^{1/2}\Omega_B U_B \\ &\quad + Re^{3/8}(U_B\widetilde{\Omega} + \widetilde{U}\Omega_B) + O(Re^{1/4}). && \text{(15b)} \end{aligned}$$

Once again, the normal components of Lamb vector l_y is much larger than the tangential component l_x. The first term in (15b) is the same as in the attached boundary layer. The other terms in (15) are the perturbation introduced by the lower deck. Remarkably, the extra l_y is of $\mathcal{O}(Re^{3/8})$, and l_x is now of $\mathcal{O}(Re^{1/4})$ instead of $O(1)$. As for the lower deck, the scale analysis gives $(u, v, \omega) = (\delta\widetilde{U}, \delta^3\widetilde{V}, \delta^{-4}\widetilde{\Omega}) + \cdots$, so that

$$(l_x, l_y) = (-Re^{1/8}\widetilde{\Omega}\widetilde{V},\ Re^{3/8}\widetilde{\Omega}\widetilde{U}) + \cdots. \qquad (16)$$

Namely, in the lower deck the normal vortex-force density is of $\mathcal{O}(Re^{3/8})$. The appearance of the lower deck enhances l_n in both the main and lower decks. Moreover, in the lower deck both u and ω have the opposite sign to that in the main deck, so that l_y has the same sign in both decks. These explain that the free shear layer just after the boundary layer separation has stronger vortex force, as has been found numerically ([27],[29]; see Fig. 11 below).

4 Total Force-Moment by Local Flow Structures

Having identified the key indicators of vortical structures and interactions, we may now study how these structures and interactions dominate the global flow performance. To this end we just need to transform the conventional performance expressions (which are some integrals) so that those indicators appear explicitly in the new integrands. In this section we illustrate the approach by considering the total force and moment acted on the body. Some other performances (not all) can be treated similarly.

4.1 Physical Constituents of Vortical Forces

In this article we call any force originating from vorticity interaction a *vortical force*, some of which were seen in our discussion of (9): the Lamb vector or vortex force, and the local time rate of circulation (vorticity). To gain an overall concept on the physical constituents of vortical forces, consider an incompressible flow over a body B which may perform arbitrary motion and deformation. We investigate this fluid-body interaction problem in a domain V_f bounded externally by a fixed control surface Σ and internally by the material body surface ∂B which has prescribed velocity distribution $\boldsymbol{u}_B$. The domain V_f is depicted in Fig. 7, whereafter $\boldsymbol{n}$ stands for the unit normal at the boundary pointing out from the fluid. Let

$$\boldsymbol{a} = \boldsymbol{u}_{,t} + \boldsymbol{\omega} \times \boldsymbol{u} + \nabla\left(\frac{1}{2}|\boldsymbol{u}|^2\right) \qquad (17)$$

be the fluid acceleration. The force exerted to the body by the fluid can be expressed as

$$\boldsymbol{F} = -\rho\int_{V_f} \boldsymbol{a}dV + \int_\Sigma(-p\boldsymbol{n} + \boldsymbol{\tau})dS, \qquad (18)$$

in which $-p\boldsymbol{n}$ and $\boldsymbol{\tau} = \mu\boldsymbol{\omega} \times \boldsymbol{n}$ are the normal and shear stresses, respectively. From this conventional formula one sees no vortical structures except the shear stress, which is typically related to boundary layers. Let us make the vortical structures appear explicitly.

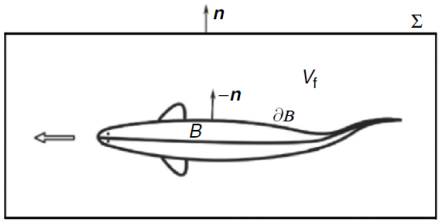

Figure 7: The sketch of the control volume and the body.

It is always possible to extend the incompressible flow field of density ρ into the material body B , as long as on ∂B the velocity and acceleration, $\boldsymbol{u}_B$ and $\boldsymbol{a}_B$, have the prescribed distributions. This continuation of the flow field into B enables writing the right-hand side of (18) in terms of a *fixed control volume* $V = V_f + B$ with only an outer boundary Σ, no matter how the material body moves and deforms in V. Then by substituting (17) into the integral of $\boldsymbol{a}$ over V, one obtains

$$\begin{aligned}\boldsymbol{F} &= -\rho\int_V \boldsymbol{u}_{,t}dV - \rho\int_V \boldsymbol{\omega}\times\boldsymbol{u}dV \\ &\quad +\rho\int_B \boldsymbol{a}_B dV + \int_\Sigma(-P\boldsymbol{n}+\boldsymbol{\tau})dS,\end{aligned}$$

where $P = p + \rho|\boldsymbol{u}|^2/2$ is the total pressure. The total vortex force shows up again.

To further exhibit the role of vortical structures in the force, recall that they are measured by the derivatives of the velocity field rather than the velocity itself. One way to reveal their role is to perform so-called *derivative-moment transformation* (*DMT*) via integral identities for arbitrary smooth vector field $\boldsymbol{f}$ and scalar field ϕ, such as

$$\begin{aligned}\int_{V_f}\boldsymbol{f}dV &= \frac{1}{k}\int_{V_f}\boldsymbol{x}\times(\nabla\times\boldsymbol{f})dV \\ &\quad -\frac{1}{k}\int_{\partial V_f}\boldsymbol{x}\times(\boldsymbol{n}\times\boldsymbol{f})dS, \qquad (19a)\end{aligned}$$

$$\int_S \phi\boldsymbol{n}dS = -\frac{1}{k}\int_S \boldsymbol{x}\times(\boldsymbol{n}\times\nabla\phi)dS, \qquad (19b)$$

in which $k = n - 1$ with $n = 2$ or 3 being the space dimension, and S is a close surface.[4] Besides, to focus on our main issue we assume temporarily that Σ is not very close to the body surface so that $\boldsymbol{\tau}$ is negligible thereon, and hence

$$\rho(\boldsymbol{u}_{,t}+\boldsymbol{\omega}\times\boldsymbol{u})+\nabla P = \boldsymbol{0} \quad \text{at } \Sigma. \qquad (20)$$

[4]The DMT theory and applications has a history of more than a century. It is not the only way to cast the integral of a variable to that of its derivatives. An alternative approach is the "projection theory", see [7].

Then, by using (19a) and (19b) to transform the volume integral of $\boldsymbol{u}_{,t}$ and boundary integral of $P\boldsymbol{n}$ in the above force formula, respectively, we obtain

$$\boldsymbol{F} = -\rho\frac{d\boldsymbol{I}}{dt}+\rho\frac{d}{dt}\int_B \boldsymbol{u}_B dV-\rho\int_V \boldsymbol{\omega}\times\boldsymbol{u}dV+\boldsymbol{F}_{\Sigma 0}, \qquad (21a)$$

in which

$$\boldsymbol{I} = \frac{1}{k}\int_V \boldsymbol{x}\times\boldsymbol{\omega}dV \qquad (21b)$$

is known as the *vortical impulse* (the first vorticity moment) in V and

$$\begin{aligned}\boldsymbol{F}_{\Sigma 0} &= \frac{1}{k}\int_\Sigma \boldsymbol{x}\times[\boldsymbol{n}\times(\rho\boldsymbol{u}_{,t}+\nabla P)]dS \\ &= -\frac{\rho}{k}\int_\Sigma \boldsymbol{x}\times(\boldsymbol{n}\times\boldsymbol{l})dS \qquad (21c)\end{aligned}$$

is a control-surface integral over Σ.

The integrand of the third terms of (21a), i.e., the total vortex force, has been discussed in § 3.1. The appearance of the forth term implies the effect of vortical wake that may extend out of Σ. If the body is stationary and the flow is steady inside V, only these two terms remain, solely in terms of the vortex force:

$$\boldsymbol{F} = -\rho\int_V \boldsymbol{l}dV - \frac{\rho}{k}\int_\Sigma \boldsymbol{x}\times(\boldsymbol{n}\times\boldsymbol{l})dS. \qquad (22)$$

It has been found that the first integral gives the lift and (in three dimensions) the inviscid induced drag, while the second one represents a viscous profile drag at finite Re that can be estimated at a wake plane [7].

In particular, in the asymptotic limit $Re \to \infty$, it is known that for two-dimensional steady flow there is no wake vortex sheet, while for three-dimensional steady flow the Lamb vector $\boldsymbol{\gamma}\times\overline{\boldsymbol{u}}$ of free vortex sheet must vanish [7]. Thus we simply have *the direct equivalence of total pressure force and vortex force*, known in various contexts since [17]:

$$\int_{\partial B} p\boldsymbol{n}dS = \rho\int_V \boldsymbol{u}\times\boldsymbol{\omega}dV, \qquad (23)$$

where $\boldsymbol{\omega}$ is actually only the vorticity inside the attached vortex sheets. Recall the remarks made in the context of (10), of which we now see that (23) is a direct generalization. It is also worth noticing that this central result in classic inviscid aerodynamics [18] can be obtained in a very neat alternative way for any "wake-free" steady flow. In fact, by the Bernoulli theorem the total pressure force on the body surface is[5]

$$\boldsymbol{F}_p \equiv \int_{\partial B} p\boldsymbol{n}dS = -\rho\int_{\partial B}\frac{1}{2}|\boldsymbol{u}|^2\boldsymbol{n}dS.$$

[5]This equation contains (10) as a special case. Thus, the algebra below also provides a simple way to rigorously derive the Kutta-Joukowski formula (26) from (10).

Now recall a classic integral identity for any vector field $\boldsymbol{f}$ over a domain $\mathcal{D}$:

$$\int_{\mathcal{D}}(\nabla\times\boldsymbol{f})\times\boldsymbol{f}dV=\int_{\partial\mathcal{D}}\left(\boldsymbol{n}\cdot\boldsymbol{f}\boldsymbol{f}-\frac{1}{2}|\boldsymbol{f}|^2\boldsymbol{n}\right)dS, \quad (24)$$

where we specify $\boldsymbol{f}$ as $\boldsymbol{u}$ and $\mathcal{D}$ as V_f in which $\boldsymbol{\omega}=\boldsymbol{0}$ except the attached vortex sheets. Since $u_n=0$ on ∂B we immediately obtain

$$\boldsymbol{F}_p=\rho\int_{\Sigma}\left(\frac{1}{2}|\boldsymbol{u}|^2\boldsymbol{n}-\boldsymbol{u}\boldsymbol{u}\cdot\boldsymbol{n}\right)dS$$

where Σ encloses $V=V_f+B$. Thus (23) follows at once by using (24) again. However, only (22) can fully clarify in what physical circumstance the "wake-free" condition holds.

Moreover, let $\boldsymbol{U}=U\boldsymbol{e}_x$ be the uniform incoming velocity and write $\boldsymbol{u}=\boldsymbol{U}+\boldsymbol{v}$ such that

$$\boldsymbol{F}_p=\rho\boldsymbol{U}\times\int_V\boldsymbol{\omega}dV-\rho\int_V\boldsymbol{\omega}\times\boldsymbol{v}dV. \quad (25)$$

Here, $\boldsymbol{v}$ is the disturbance velocity induced by the vorticity, i.e., $\boldsymbol{\omega}=\nabla\times\boldsymbol{v}$. Then by using the Biot-Savart formula for $\boldsymbol{v}$, reference [18] has elegantly proved that *in and only in* two-dimensional flow the above second integral vanishes identically provided that $\boldsymbol{\omega}$ and $\boldsymbol{v}$ span the same V. Therefore, the Kutta-Joukowski formula follows from (25) at once:

$$\boldsymbol{F}=\rho\boldsymbol{U}\times\boldsymbol{\Gamma}\ \text{ with }\ \boldsymbol{\Gamma}=\boldsymbol{e}_z\int\omega dV,\quad \text{or}\ \ F_y=-\rho U\Gamma, \quad (26)$$

where Γ is the total vorticity inside the attached vortex sheets.

We now turn to the first term of (21a),

$$-\rho\frac{d\boldsymbol{I}}{dt}=-\frac{\rho}{k}\int_V\boldsymbol{x}\times\boldsymbol{\omega}_{,t}dV, \quad (27)$$

which plays a role somehow similar to the unsteady term in (9). It is especially useful for pinpointing the local regions where the vortical flow unsteadiness is maximal or the source of it (by surveying the time evolution of the flow). For example, the spontaneous unsteadiness caused by vortex instability and breakdown has been a major concern in various practical problems. Then, when the body has non-inertial motion and deformation, the second term of (21a) appears. It is a familiar inertial force due to the acceleration of the fluid displaced by B, but not the virtual-mass effect caused by the body acceleration. The latter is conventionally explained by a non-cyclic potential-flow model, but actually has been included in (27) as proved in [30] and [7]. Therefore, we may say that all incompressible aerodynamic forces are vortical.

Finally, when V expends to the entire space V_∞ with the fluid at rest or uniform motion at infinity such that the starting vortex system is also enclosed, by (24) it can be easily shown that the total vortex force disappears. Then (21a) reduces to

$$\boldsymbol{F}=-\rho\frac{d\boldsymbol{I}_\infty}{dt}+\rho\frac{d}{dt}\int_B\boldsymbol{u}_BdV, \quad (28)$$

where $\boldsymbol{I}_\infty$ denotes the vortical impulse in V_∞. This elegant formula is the very basis of the Burgers-Wu-Lighthill *vorticity-moment (impulse) theory* ([31]-[33]), where the flow is surely unsteady. The conditions for (22) and (28) are mutually exclusive. The vorticity-moment theory may find extensive applications in the study of the motion of fish, insects, and birds (e.g., [34]); but since in practice it is impossible to measure or calculate the flow data in the entire V_∞, (28) needs to be and has been generalized to a form suitable to finite domain [7].

4.2 Force-Moment by Advection vs Diffusion

In what follow we remove the preceding simplified assumption that $\boldsymbol{\tau}$ is negligible on Σ, and present completely general force and moment formulas to be used in engineering applications. We also give their generalization to compressible flow. The flow domain V_f is still shown by Fig. 7. The emphasis is on the inherent relations of different expressions. For their derivations see [7] and [29].

We start again from (17). In general, we find that $\boldsymbol{F}$ has three constituents, a volume integral over V_f, a body-surface integral over ∂B, and a control-surface integral over Σ. We thus write

$$\boldsymbol{F}=\boldsymbol{F}_V+\boldsymbol{F}_B+\boldsymbol{F}_\Sigma. \quad (29)$$

Here, the two surface integrals are found to be

$$\boldsymbol{F}_B=\frac{1}{k}\int_{\partial B}\rho\boldsymbol{x}\times\boldsymbol{\sigma}_adS, \quad (30a)$$

$$\boldsymbol{F}_\Sigma=-\frac{\mu}{k}\int_\Sigma\boldsymbol{x}\times[\boldsymbol{n}\times(\nabla\times\boldsymbol{\omega})]dS+\int_\Sigma\boldsymbol{\tau}dS, \quad (30b)$$

where we recall that $\boldsymbol{\sigma}_a=\boldsymbol{n}\times\boldsymbol{a}_B$ is the BVF due to body-surface acceleration, $\boldsymbol{\tau}=\mu\boldsymbol{\omega}\times\boldsymbol{n}$ is the shear stress, and $k=n-1$ with $n=2,3$ being the space dimension. The volume integral can be alternatively expressed as

advection form and diffusion form:

$$\begin{aligned} \boldsymbol{F}_V &= -\frac{\rho}{k}\int_{V_f} \boldsymbol{x}\times\boldsymbol{\omega}_{,t}dV - \rho\int_{V_f}\boldsymbol{l}dV \\ &\quad -\frac{\rho}{k}\int_{\partial V_f}\boldsymbol{x}\times(\boldsymbol{n}\times\boldsymbol{l})dS \qquad (31a) \\ &= -\frac{\mu}{k}\int_{V_f}\boldsymbol{x}\times\nabla^2\boldsymbol{\omega}dV, \qquad (31b) \end{aligned}$$

of which the equivalence is evident if one recalls the vorticity transport equation (3a) and the DMT identity (19a). The sum of vortex force and unsteady force in the advection form, discussed in the preceding subsection, gives the diffusion form.

At $Re \gg 1$, a flow field created by a body motion may be generally divided into three regions. In the outer and largest region the flow is irrotational and effectively inviscid. In the small inner region close to the body there are boundary layers and separated shear layers, where the flow is both rotational and viscous. In between of the two is an effectively inviscid and rotational region, the wake. Thus, following the learning order of the aforementioned observer, one would first see the strongest axial vortices signified by the integrands of the advection form (31a), and then free and attached shear layers signified by the integrand of the diffusion form (31b). Only in the inner region the two inviscid terms $\boldsymbol{\omega}_{,t}$ and $\nabla\times\boldsymbol{l}$ of (3a) do not cancel out but equals an appreciable viscous term $\nu\nabla^2\boldsymbol{\omega}$.

The situation can be illustrated by the unsteady separated flow over a circular cylinder. Figure 8 plots the contours of the integrands in the volume integrals of (31a) in the vortical wake region. All wake vortices are obviously involved, but as a vortex moves downstream both $\boldsymbol{\omega}_{,t}$ and vertical velocity v change sign at a spatial point, so that the Lamb vector in each vortex has both the positive and negative contributions to $\boldsymbol{F}_V$, which are largely canceled. This fact has been quantitatively confirmed [29]. The remaining net contribution to $\boldsymbol{F}_V$ is nothing but that given by the integrand of (31b), which captures precisely the attached boundary layers and free separated shear layers before the latter roll into axial vortices. This is shown in Fig. 9 for the same cylinder flow. Therefore, it suffices to focus on the near-wake region before the wake vortices are formed and shed into the Kármán street.

For the total moment we have similar results. We start from

$$\boldsymbol{M} = -\rho\int_{V_f}\boldsymbol{x}\times\boldsymbol{a}dV + \int_\Sigma \boldsymbol{x}\times(-p\boldsymbol{n}+\boldsymbol{\tau})dS + \boldsymbol{M}_{s\Sigma}, \qquad (32a)$$

where there is an extra viscous term (for the origin see,

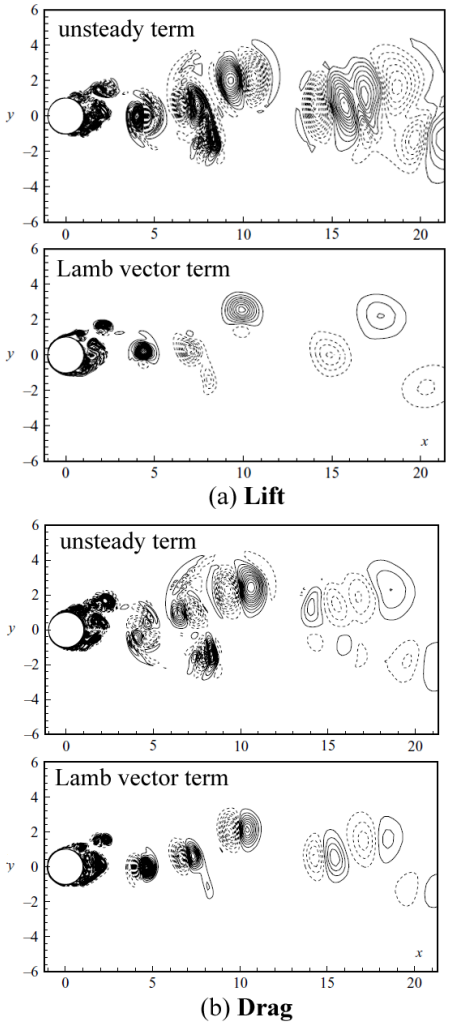

Figure 8: Contours of the volume integrands in (31a) for flow over circular cylinder [29].

e.g. [7], § 2.4.2)

$$\boldsymbol{M}_{s\Sigma} = -2\mu\int_\Sigma \boldsymbol{n}\times\boldsymbol{u}dS = -2\mu\int_V \boldsymbol{\omega}dV. \qquad (32b)$$

The DMT identity for transforming (32a) is

$$2\int_{V_f}\boldsymbol{x}\times\boldsymbol{f}dV = -\int_{V_f}x^2\nabla\times\boldsymbol{f}dV + \int_{\partial V_f}x^2\boldsymbol{n}\times\boldsymbol{f}dS. \qquad (33)$$

Then we write

$$\boldsymbol{M} = \boldsymbol{M}_V + \boldsymbol{M}_B + \boldsymbol{M}_\Sigma, \qquad (34)$$

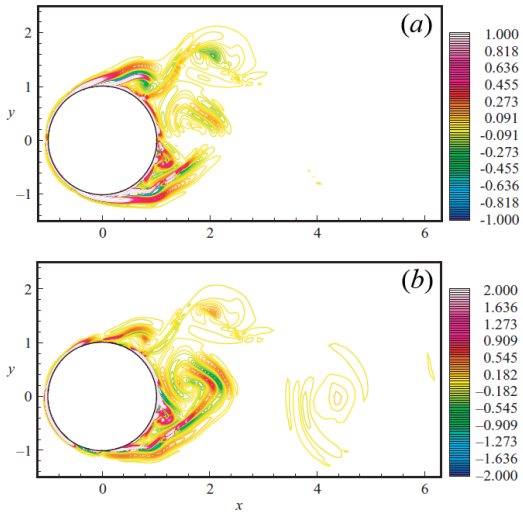

Figure 9: The contours of the integrand in (31b) for flow over circular cylinder [29]. (a) the drag component and (b) the lift component. The total range of the value is $[-64, 183]$ for (a) and $[-343, 238]$ for (b).

where

$$\boldsymbol{M}_B = -\frac{1}{2}\int_{\partial B} \rho x^2 \boldsymbol{\sigma}_a dS, \tag{35a}$$

$$\boldsymbol{M}_\Sigma = \frac{\mu}{2}\int_\Sigma x^2 \boldsymbol{n}\times(\nabla\times\boldsymbol{\omega})dS + \int_\Sigma \boldsymbol{x}\times\boldsymbol{\tau}dS + \boldsymbol{M}_{s\Sigma}, \tag{35b}$$

and

$$\boldsymbol{M}_V = \rho\int_{V_f}\left(\frac{1}{2}x^2\boldsymbol{\omega}_{,t} + \boldsymbol{x}\times\boldsymbol{l}\right)dV + \frac{1}{2}\int_{\partial V_f} x^2\boldsymbol{n}\times\boldsymbol{l}dS \tag{36a}$$

$$= \frac{\mu}{2}\int_{V_f} x^2\nabla^2\boldsymbol{\omega}dV. \tag{36b}$$

In practical applications the body surface ∂B and/or control surface Σ on which the flow is to be analyzed could be open, bounded by closed boundary curves. This situation occurs if one's concern is the aerodynamics force of a wing alone rather than a whole aircraft, or the total moment of the rotor or runner blades in turbo flows rather than the whole rotating part. In this case extra line integrals along the boundary loops of open surfaces have to be added. The extension of the above expressions to this situation has been given by [29].

4.3 Force-Moment by BVF

If the aforementioned observer wishes to trace further from near-wall shear layers to their on-wall physical root, he or she would come to the force-moment expressions solely in terms of on-wall vortical quantities. The Lamb vector disappears, and the integrands are in terms of the BVF $\boldsymbol{\sigma}$ and boundary vorticity $\boldsymbol{\omega}_b$. The desired expressions can be obtained by shrinking the control surface Σ to collapse to the body surface ∂B with $V_f \to 0$. Note that the normal vectors of the two surfaces were in the opposite directions, i.e. $\boldsymbol{n}_{\partial B} = -\boldsymbol{n}_\Sigma$. In keeping with our convention that $\boldsymbol{n}$ is the normal pointing out of the fluid, it follows that

$$\boldsymbol{F} = \frac{1}{k}\int_{\partial B}\rho\boldsymbol{x}\times[\boldsymbol{\sigma}_a + \nu\boldsymbol{n}\times(\nabla\times\boldsymbol{\omega})]dS + \int_{\partial B}\boldsymbol{\tau}dS, \tag{37}$$

$$\boldsymbol{M} = -\frac{1}{2}\int_{\partial B}\rho x^2[\boldsymbol{\sigma}_a + \nu\boldsymbol{n}\times(\nabla\times\boldsymbol{\omega})]dS - \int_{\partial B}\boldsymbol{x}\times\boldsymbol{\tau}dS - 2\mu\int_B\boldsymbol{\omega}dV. \tag{38}$$

By the identity

$$\boldsymbol{n}\times(\nabla\times\boldsymbol{\omega}) = -\frac{\partial\boldsymbol{\omega}}{\partial n} + (\boldsymbol{n}\times\nabla)\times\boldsymbol{\omega}$$

and boundary coupling relation (4b), and using the notation of (5b), these formulas are reduced to

$$\boldsymbol{F} = -\frac{1}{k}\int_{\partial B}\rho\boldsymbol{x}\times\boldsymbol{\sigma}_p dS + \int_{\partial B}\boldsymbol{\tau}dS, \tag{39}$$

$$\boldsymbol{M} = \frac{1}{2}\int_{\partial B}\rho x^2\boldsymbol{\sigma}_p dS + \int_{\partial B}\boldsymbol{x}\times\boldsymbol{\tau}dS - 2\mu\int_B\boldsymbol{\omega}dV. \tag{40}$$

The main contributor to $\boldsymbol{F}$ and $\boldsymbol{M}$ is the moments of pressure-gradient caused BVF, $\boldsymbol{\sigma}_p = \mathcal{O}(1)$. In and only in three-dimensional flow, the integrals of shear stress $\boldsymbol{\tau}$ and its first moment can be cast to those of the first and second moments of the viscous BVF, $\boldsymbol{\sigma}_v$, by some other DMT identities [7]. Then $\boldsymbol{F}$ and $\boldsymbol{M}$ are expressible solely in terms of BVFs. But in practical flow diagnoses and optimal configuration designs at sufficiently large Re, it is usually sufficient to consider only the inviscid portion of these expressions.

Equations (39) and (40) can also be extended to open body surface with closed boundary loop. Relevant extra line integrals have been given by [7], § 11.4.1.

4.4 Extension to Compressible Flow

Incompressible flow is a model flow in which not only the thermodynamic process is completely decoupled but also

the coupling between compressing and shearing process is minimal and occurs merely at boundary. The role of pressure can be entirely eliminated in the interior of the flow. Once we enter compressible flow, the interior coupling of the three processes takes place and becomes stronger as the Mach number increases. But some of the preceding force-moment expressions remain unchange, provided that μ is still assumed constant. These include the expressions of $\boldsymbol{F}_B$ and $\boldsymbol{F}_\Sigma$ and their counterparts for the moment, and the diffusion form of $\boldsymbol{F}_V$ and $\boldsymbol{M}_V$. Only their advection form needs to be revised. For example, (31a) should be generalized to ([7],[29])

$$\boldsymbol{F}_V = -\frac{1}{k}\int_{V_f} \boldsymbol{x}\times\nabla\times(\rho\boldsymbol{u}_{,t})dV - \int_{V_f}\left(\rho\boldsymbol{l}-\frac{1}{2}|\boldsymbol{u}|^2\nabla\rho\right)dV$$
$$-\frac{1}{k}\int_{\partial V_f}\boldsymbol{x}\times\left[\boldsymbol{n}\times\left(\rho\boldsymbol{l}-\frac{1}{2}|\boldsymbol{u}|^2\nabla\rho\right)\right]dS. \qquad (41)$$

In this formula, the integrands $\rho\boldsymbol{l}$ and $|\boldsymbol{u}|^2\nabla\rho/2$ are dominated by the shearing and compressing processes, respectively (still with some cross coupling, since ρ is a compressing variable and $\boldsymbol{u}$ comes from both). The unsteady term is a combination of both processes. In contrast to the vortex force $\rho\boldsymbol{l}$ (per unit volume) that always produces a force lateral to both local velocity and vorticity, the "compressing force" $|\boldsymbol{u}|^2\nabla\rho/2$ always produces a force pointing to the local density increment direction. This is true not only across shock waves but also in the entire range of local Mach-number M from subsonic to supersonic flows. For example, in a steady one-dimensional fluid tube of variable sectional area A, the "compressing force" acting to the *fluid* element is

$$dF_f = -\frac{1}{2}u^2 d\rho = -\frac{1}{2}\rho u^2\frac{M^2}{1-M^2}\frac{dA}{A}. \qquad (42)$$

Thus, we have $dF_f > 0$ or the fluid is accelerated if either $M<1$ and $dA<0$ or $M>1$ and $dA>0$ as it should be.

We remark that although (41) is an exact formula and can be conveniently used in complex flow diagnosis, it is not yet the final result. The density variation may still be split to an isentropic part (which amounts to the variation of local Mach number) and an entropy-caused part, of which a detailed identification could be desired. We leave this issue to future study.

5 Complex Flow Diagnosis and Optimization

The preceding sections, developed from the general theory on multi-process decomposition and coupling, form a quite systematic theoretical framework for complex flow diagnosis and optimization, which may be called *local dynamics theory* for short. In this section we show a set of examples of significant practical value where the LDT plays an indispensable role.

5.1 Delta-Wing Flows

Reference [27] conducted a diagnosis of the steady flow over a delta wing of sweep angle $\Lambda = 76^\circ$ at the angle of attack $\alpha = 20^\circ$. The Reynolds number based on the root-chord length c and uniform incoming velocity U is $Re = 5\times10^5$. The typical vorticity distribution on a sectional plane $x/c = 0.8$ is plotted in Fig. 10. Obviously, the axial-vorticity ω_x concentrates in boundary layers, separated shear layers and the primary vortex. In each axial vortex (e.g., the primary and the secondary vortices) the vorticity is nearly along the axial direction, so on sectional planes perpendicular to the vortex axis the velocity takes opposite signs at the different sides of the axis. As a result, the distributions of the Lamb vector components in each axial vortex are divided into two parts with different signs, as shown in Fig. 11 for l_x and l_z on the same sectional plane.

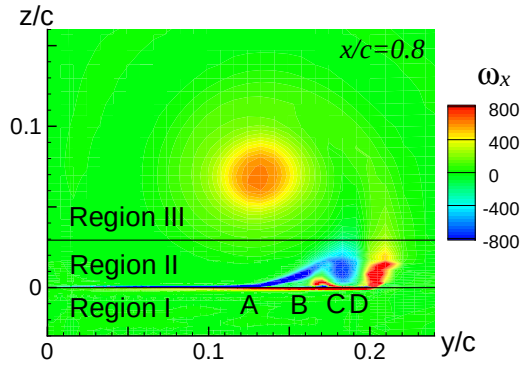

Figure 10: Contours of the axial vorticity ω_x on the cross section $x/c = 0.8$, where A, B, C and D denote secondary separation, tertiary reattachment, tertiary separation and secondary reattachment, respectively [27].

In [27], formula (22) has been used to quantitatively identify the contributions of various vortical structures to the aerodynamic forces. These structures were distinguished by dividing the flow domain into three subdomains and then calculating the integrals in (22) separately. As indicated in Fig. 10; Region I with $z<0$ contains the attached boundary layer of the lower wing surface, Region II contains the attached boundary layer of the upper surface, the secondary and tertiary separated vortices, and the initial portion of the free shear layer; and Region III contains the main leading-edge vortex and the feeding shear layer outside Region II. Figure. 12 plots

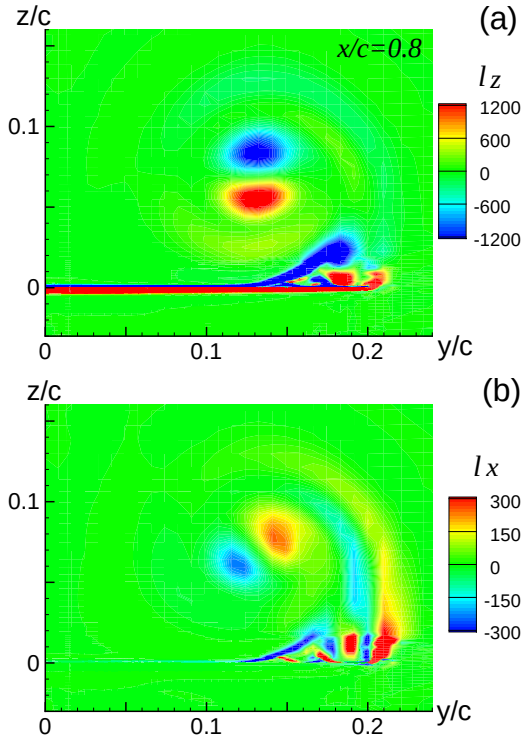

Figure 11: Contours of the normal component of Lamb vector l_z (a) and the axial component l_x (b) on the cross section $x/c = 0.8$ [27].

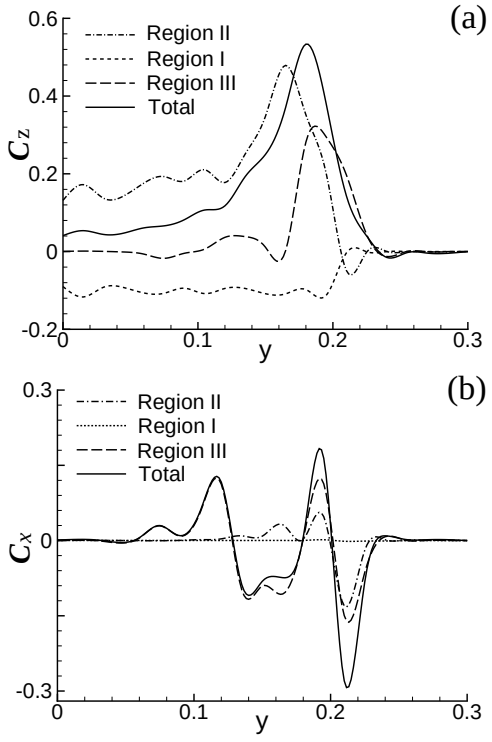

Figure 12: Spanwise contributions of the normal force coefficient C_z (a) and the axial force coefficient C_x (b) at the section $x/c = 0.8$ [27].

the spanwise distributions of these contributions to the normal and axial force coefficients on the section $x/c = 0.8$. The lift has two major sources from Region II and III, i.e., the free shear layers formed after the separation of the upper boundary layer and before joining the secondary separated vortices, and the feeding shear layer of the main vortices, respectively. The axial vortices make small contribution due to the Lamb-vector cancelation among its opposite-sign regions seen in Fig. 11. The upper and lower attached boundary layers have positive and negative contributions. Although these different structures lead to an uneven spanwise distributions in Fig. 12(b), the total or net axial force is rather small.

The above diagnosis contradicts one's conventional understanding that the leading-edge vortices themselves provide the major additional lift at large α (in fact, so far no exact theory can prove this assertion), but confirm our general observation on the advection and diffusion forms of the vortical forces (§ 4.2). However, it is these axial vortices that change the behavior of other flow structures including inducing the separation of the upper boundary layer. The shear layer formed thereafter produces large vortex force, which is related to the curve of Region II in Fig. 12. But as soon as this shear layer rolls into the secondary vortex, it again contributes little to the vortex force.

An unsteady flow over a delta wing of moderate sweeping angle $\Lambda = 50°$ at $\alpha = 15°$ has been diagnosed by [36] based on (31a). The flow unsteadiness is caused spontaneously by the high-frequency shear-layer instability ($St \sim 10$) and vortex breakdown, the latter including unsteady modes in breakdown regions ($St \sim 1$) and fluctuation of breakdown location ($St \sim 0.1$). The main causes of the total force are the two volume integrals in (31a). Their integrand distributions on two sectional planes at $x/c = 0.2$ (before breakdown) and 0.7 (after breakdown), both the axial and normal components, are shown in Fig. 13, where the time-averaging was made over short waves to remove high-frequency fluctuations (of which the instantaneous peaks of $\boldsymbol{\omega}_{,t}$ were found to be larger than its short-wave average by 2 to 3 orders) and retain only the effect of lowest-frequency ($St \sim 0.1$). The Lamb vector overwhelms the short-wave averaged unsteady vortical force both before and after the vortex breakdown; but itself is somewhat reduced after breakdown that loosens the axial vortices.

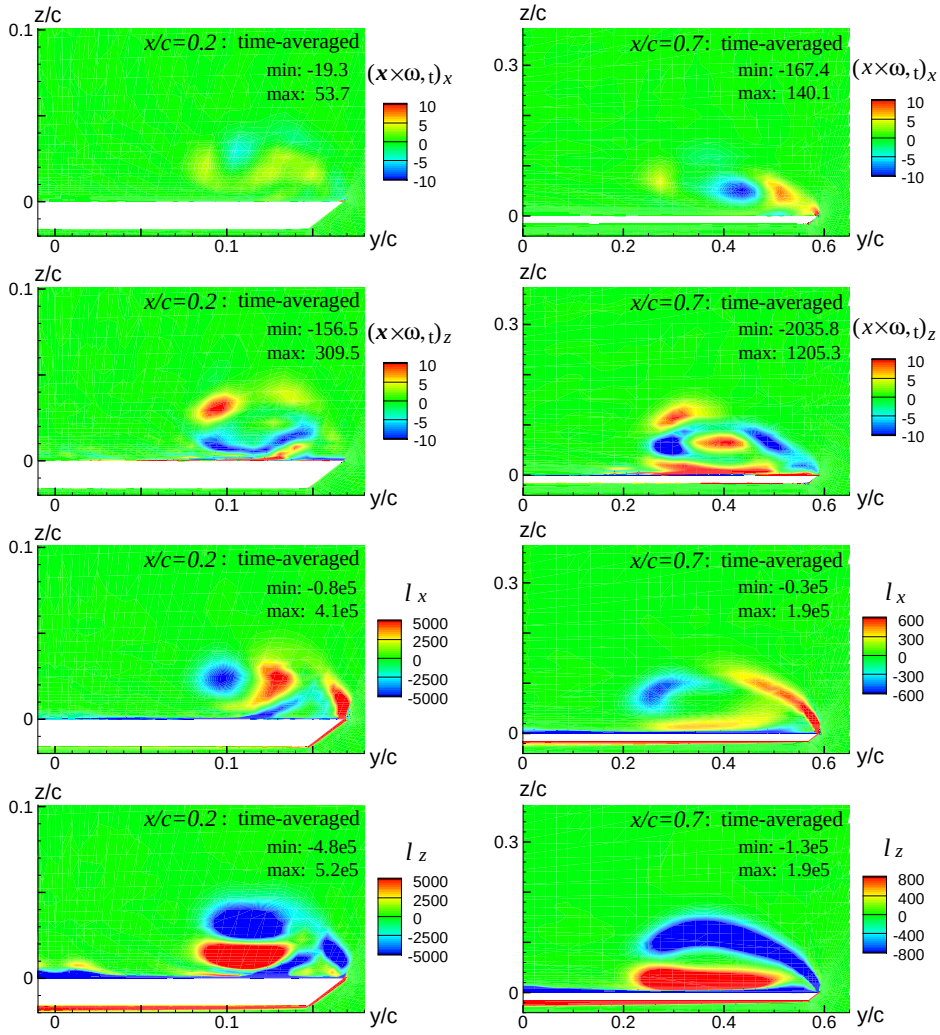

Figure 13: The distributions of the x and z components of $\boldsymbol{x} \times \boldsymbol{\omega}_{,t}$ and $\boldsymbol{l}$ at $x/c = 0.2$ (left column) and $x/c = 0.7$ (right column), averaged over time [36]. The figures on the left are more magnified than those on the right.

5.2 Compressible Flow Over Wavy Cylinder

Bluff-body flow is one of the most important types of complex flows. Its management aiming at reducing the drag and suppressing the flow fluctuation is of considerable interest at both fundamental and applied levels. While most existing investigations have focused on flow over straight cylinders, flow over a wavy cylinder whose diameter varies sinusoidally along the span has recently caught significant attentions due to its lower drag and force fluctuations. Wavy cylinder could become a prototype configuration for the study of bluff-body flow management. The relevant progress has been reviewed by [35], who made a large-eddy simulation and analysis of a compressible flow past a wavy cylinder at free-stream Mach number $M_\infty = 0.75$ and Reynolds number $Re = 2\times 10^5$ based on the mean diameter D. The wave amplitude and spanwise wavelength are $0.1D$ and $2D$, respectively. The flow complexities come from both shearing and compressing processes as well as their coupling, both inside the flow field and on cylinder surface. Here we outline those findings of [35] relevant to our vortical flow diagnosis and add a few short discussions.

By using the compressible force formula (41) (with proper line integrals added along the boundaries of the open end surfaces of the cylinder), it has been found that the time-average drag is reduced by 26% compared to the straight cylinder, and the lift fluctuation is suppressed by over an order. The compressing and shearing sources of the drag were assessed by calculating the following

regrouped terms in (41):

$$\boldsymbol{F}_{\rm comp} = \frac{1}{2}\int_{V_f} |\boldsymbol{u}|^2 \nabla\rho dV + \frac{1}{2}\int_{\partial V_f} \boldsymbol{x}\times\left(\boldsymbol{n}\times\frac{1}{2}|\boldsymbol{u}|^2\nabla\rho\right) dS, \qquad (43)$$

$$\boldsymbol{F}_{\rm shear} = -\int_{V_f} \rho\boldsymbol{l} dV - \frac{1}{2}\int_{\partial V_f} \boldsymbol{x}\times(\boldsymbol{n}\times\rho\boldsymbol{l})\, dS. \qquad (44)$$

For the straight cylinder, the drag coefficients given by $\boldsymbol{F}_{\rm comp}$ and $\boldsymbol{F}_{\rm shear}$ are 0.45 and 0.34, respectively, indicating that the compressing process produces more drag than shearing process for this case. For the wavy cylinder, these two values are 0.35 and 0.24, with reductions of 22% and 29%, respectively. Thus, the drag reduction due to the shearing process prevails over that due to the compressing process in this flow. Now the question is why.

A direct reason for the reduction of $\boldsymbol{F}_{\rm comp}$ and $\boldsymbol{F}_{\rm shear}$ on wavy cylinder is the appearance of the spanwise components of $\nabla\rho$ and the vortex force $-\rho\boldsymbol{l} = \rho(\boldsymbol{u}\times\boldsymbol{\omega})$ which are eventually canceled because of the periodic flow conditions in that direction. Thus, for the same $|\boldsymbol{u}|^2|\nabla\rho|$ and $\rho|\boldsymbol{u}\times\boldsymbol{\omega}|$, the drag and lift on the wavy cylinder will be smaller. Besides, one more mechanism is the reduction of the angle between $\boldsymbol{u}$ and $\boldsymbol{\omega}$ (say β) from $\pi/2$ as pointed out in § 3.1. In fact, on the wavy cylinder the mean-flow separation line is also wavy [35], implying that in the separated shear layers β must decrease. The locations where β is significantly reduced may be identified by the magnitude of the helicity density $|\boldsymbol{\omega}\cdot\boldsymbol{u}|$ (not shown here). This additional mechanism existing in vortex force only should be a cause of more drag reduction in the shearing process than that in the compressing.

To make more detailed diagnosis of the physics behind the drag and fluctuation reduction, Fig. 14 depicts the computed wake vortices defined by the the Q-criterion (cf. [7]). A prominent change is that at the near-wake region the vortical structures are much less active behind the wavy cylinder than that behind the straight one. This fact can also be seen from distributions of $\nabla\cdot\boldsymbol{l}$ in the cross-section planes, Fig. 15. The two-layers structures with positive and negative values capture the free shear layers. Clearly, for the wavy cylinder the shear layers are more stable and extend to much more downstream locations than that separated from the straight cylinder.

A closer inspection of the wake-structure evolution by [35] has further revealed that the main cause of the above wake-pattern change should be attributed to the postponed and weakened roll-up process of the separated shear layers, compared with the straight cylinder. This is precisely what one may anticipate based on the argument

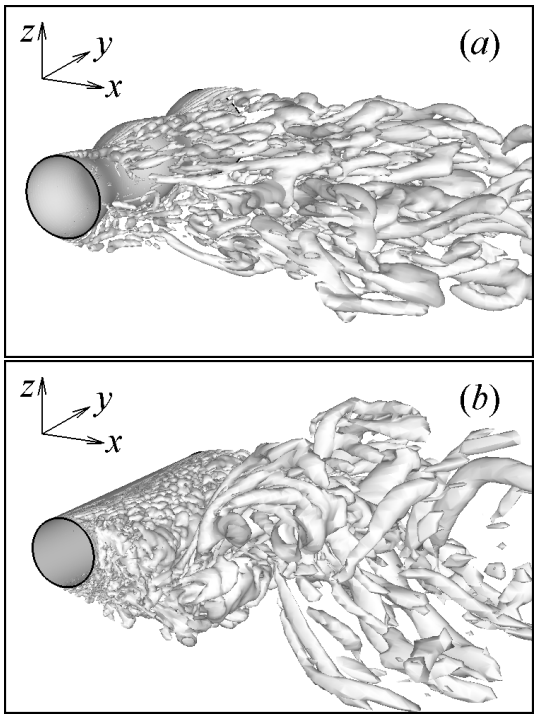

Figure 14: The vortices illustrated by the Q-criterion (Q is assigned to the same value in both plots): (a) wavy cylinder, (b) straight cylinder [35].

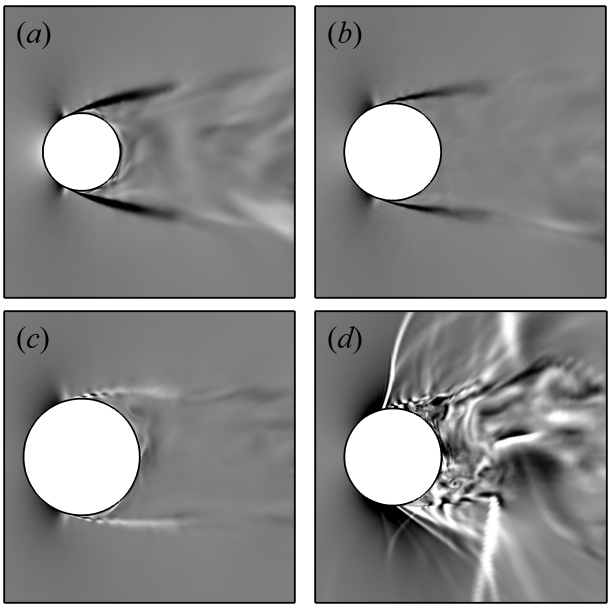

Figure 15: The instantaneous distributions of the Lamb-vector divergence in cross-sections: (a) location with maximum diameter, (b) location with middle diameter, (c) location with minimum diameter, and (d) straight cylinder [35].

at the end of § 3.2. As a result of the β decrease between $\boldsymbol{u}$ and $\boldsymbol{\omega}$, not only is $\boldsymbol{F}_{\rm shear}$ reduced but also the roll-up process becomes milder or weaker. When β reduces to zero the roll up cannot happen at all. This situation can be clearly understood by comparing the vortex systems generated by a rectangular wing of large aspect ratio and a slender wing of small aspect ratio, both at large angles of attack; so far as their respective vortex systems are concerned, these wing flows are the analogies of the straight cylinder and wavy cylinder of one wavelength. Consequently, for the wavy cylinder, the longer downstream extension and delayed/weakened roll up of the free shear layers lead to smaller and more streamwise-oriented axial vortices, which in turn result in the elimination of shocks and shocklets in the wake region as observed by [35]— another reason for the reduction of $\boldsymbol{F}_{\rm comp}$.

5.3 Optimal Design of Compressor Rotor Blade

Turbo flow is a highly important but very difficult area in complex flow diagnosis and management. The global performance of turbo-machines involves inevitably the total force and especially the total moment, but one's ultimate concern is some other criteria, for example the stagnation-pressure ratio (SPR) and efficiency of a turbofan compressor, defined by proper flow integrals over sectional planes at inlet and exit of the compressor. In this case a simple derivative-moment transformation other than those used in § 4 can be applied to expose the role of vortical-flow structures and their couplings with compressing process in relevant integrals. For example, in terms of cylindrical coordinates (r, θ, z), let S_0 be a sectional plane at $z = z_0$, and $R_1(z)$ and $R_2(z)$ be the generators of the hub and shroud, respectively. The integral of variable $f(r, \theta, z)$ over S_0 can then be cast to the r-moment of $\partial f/\partial r$ [37]:

$$\int_{S_0} f r dr d\theta = \frac{1}{2}\left[\int_0^{2\pi} (fr^2)\Big|_{R_1}^{R_2} - \int_{S_0} r^2 \frac{\partial f}{\partial r} dr d\theta\right] \quad (45)$$
$$\text{at} \quad z = z_0.$$

Thus, for a unidirectional and axisymmetric flow, the mass flux can be cast to

$$Q = \int_{S_0} \rho u_z dS = \frac{1}{2}\int_S r\rho\omega_\theta dS,$$

indicating that the mass flux is dominated by the r-moment of the azimuthal vorticity, which has high peak in boundary layer. One may then immediately realize that boundary-layer separation could reduce this ω_θ-moment and hence the mass flux.

Similarly, a combination of (45) and the NS equations can cast the stagnation-pressure flux (SPF) to a form in which the integrand is mainly the r-moment of the r-component of the Lamb vector, $l_r = \omega_\theta u_z - \omega_z u_\theta$. A three-dimensional numerical investigation [38] and a theoretical analysis [37] on an axisymmetric through-flow model have both confirmed that of the two terms of l_r the ω_θ-term is again dominant. Namely, one has

$$\begin{aligned} \text{SPF} &= \int_S P^* u_z dS \\ &= \frac{1}{2}\int_S r^2 (P^* + \rho u_z^2)\omega_\theta dr d\theta + \text{small terms}, \end{aligned} \quad (46)$$

where P^* is the stagnation pressure. Therefore, ideally, the optimal ω_θ-distribution would be to concentrate in the large-r region, i.e., like the mass flux, ω_θ should vanish in the effectively inviscid core flow and only peak in the boundary layers adjacent to the hub and shroud that should remain attached. While this optimal distribution can hardly be achieved in reality, embedding it into the primary design procedure can yield an optimal yet preliminary blade geometry. A three-dimensional numerical verification has then shown that, compared with the conventional preliminary design, this approach raises the peak values of the SPR and efficiency by 1.7% and 1.1%, respectively [37].

Then, as one enters the three-dimensional compressor flow diagnosis and detailed design, one may optimize the axial moment exerted to the fluid by rotor blades. After neglecting all viscous terms and adding a line integral for open surface in the BVF-based moment formula (40), this axial moment reads

$$M_z|_{\text{to fluid}} = -M_z = -\frac{1}{2}\int_{\partial B} \rho r^2 \sigma_{pz} dS + \frac{1}{2}\oint_{\mathcal{C}} p r^2 dz, \quad (47)$$

where the closed-line integral is along both the top and root boundary curves of the blade's open surface ∂B which dominates the local contribution to M_z there. Reference [26] has utilized (47) to diagnose the transonic flow around the blade. The distribution of σ_{pz} on the suction side of the original blade is shown in Fig. 16(a). A large positive peak appears at the middle region, where locates a strong tangential pressure gradient along the chord direction induced by a shock wave. This shock wave causes a boundary-layer separation indicated by the local $(\boldsymbol{\sigma}_p, \boldsymbol{\tau})$ alignment criterion (§ 3.4), as has been shown in Fig. 5. The boundary-layer separation weakens the SPR and efficiency. The rotor performance will be enhanced by minimizing the separation zones and the BVF peak, which will in turn increase $M_z|_{\text{to fluid}}$.

To this end, an optimal-design method has been developed to maximize the first integral of (47) on a

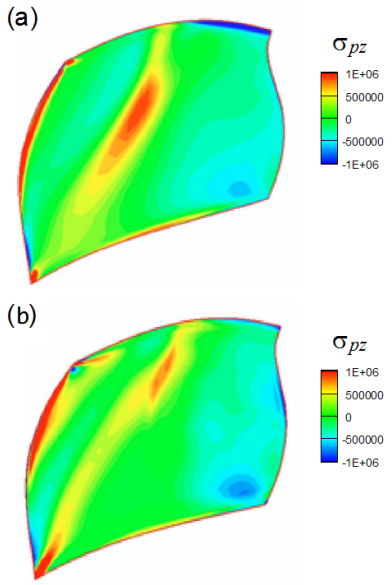

Figure 16: (a) Axial BVF (σ_{pz}) on the suction side of an original compressor's rotor blade; (b) σ_{pz} on an optimized blade's suction side [26].

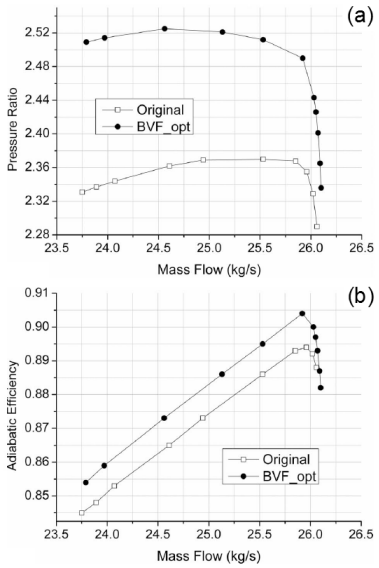

Figure 17: The performance comparison of the original and the BVF-optimized rotor blade [26]: (a) pressure ratio; (b) adiabatic efficiency.

set of sectional foils at the middle part of S, and the second integral on the tip and root [26]. Fig.16(b) presents the axial BVF distribution on the suction side of the optimized blade. The unfavorable positive peak of σ_{pz} in Fig.16(a) was weakened and shifted downstream, indicating that the shock wave and its induced separation was significantly suppressed. As a result, the axial moment was increased by 6%, and at the rotor's peak-efficiency point the SPR and adiabatic efficiency were increased by 5.73% and 1.11%, respectively, see Fig. 17.

5.4 Optimal Design of Wind-Turbine Blades

The same axial-moment formula (47) has also been used by [36] to diagnose the wind-turbine flow field and perform optimal design, the only difference being that now the moment M_z acting to the turbine blade needs to be maximized.

The prototype of the configuration was a NERL phase VI wind-turbine blade. The design variable was chosen as sectional twist-angle distribution along the blade span, for which an optimization procedure has been devised. The blade sectional foil profiles were kept the same as NERL phase VI. The vector lines of the BVF $\boldsymbol{\sigma}_p$ and skin-friction $\boldsymbol{\tau}$ on the blade surface before and after optimization are shown in Fig. 18. The $\boldsymbol{\tau}$-lines signify the flow directions adjacent to the wall, and as before three-dimensional boundary-layer separation was identified at the blade surface region where the $\boldsymbol{\sigma}_p$-lines become nearly aligned to the $\boldsymbol{\tau}$-lines. On the prototype blade this happens at about 45% to 90% spanwise locations, which is significantly postponed on the optimized configuration. Correspondingly, Fig. 19(a) shows the improvement of the spanwise distribution of sectional axial-moment due to the great reduction of the boundary-layer separation zone, at wing speed $W = 10m/s$. In fact, this improvement occurs in a wide wind-speed range $W = 10m/s$ to $25m/s$, during which the total axial moment (shaft torque, or the power generation) is increased by 13.1% to 36.2%, as shown in Fig.19(b).

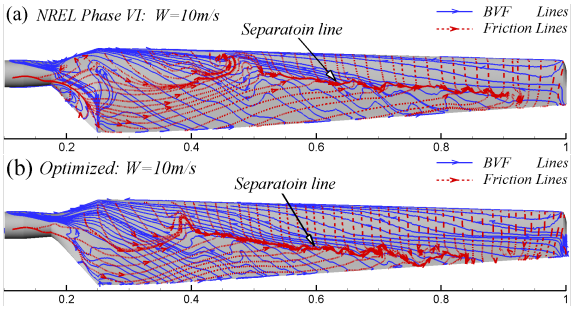

Figure 18: Distribution of friction lines (dotted) and BVF lines (solid) on the blade's suction side under the wind speed $W = 10m/s$: (a) the original blade (NREL phase VI); (b) the optimized blade [36].

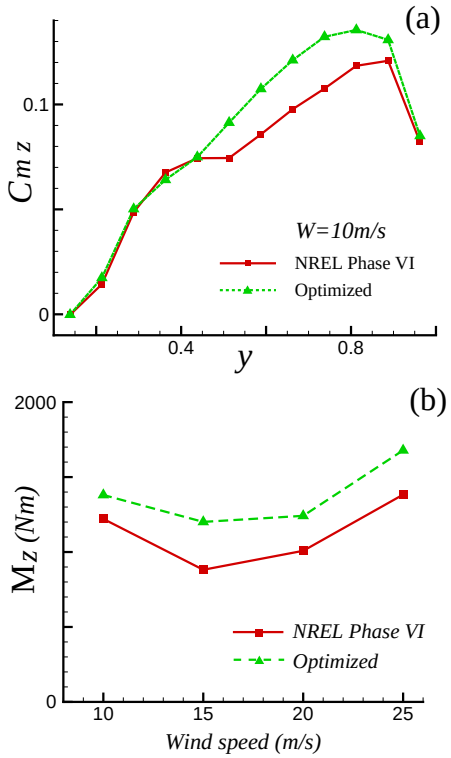

Figure 19: Comparison of the blade's aerodynamic performances: (a) Spanwise distributions of axial-moment coefficient at $W = 10m/s$; (b) Total axial moments (shaft torques) versus wing speed [36].

5.5 Instability and Optimal Design of Francis Turbine

Operational stability is always a key performance requirement for various fluid machines. Vortex instability and breakdown is one of the major causes for a fluid machine with vortical flow to lose its operational stability. The vortex breakdown on a delta wing of moderate sweep angle at large angles of attack, as we encountered in § 5.1, is a familiar example. Another typical example of similar kind in turbo flows is the severe low-frequency pressure fluctuation of Francis water turbine at off-design condition. Both model tests and numerical simulations suggested that this fluctuation is associated with some unsteady "vortex ropes" in the draft tube. Although a few engineering methods such as air admission at the draft-tube inlet had been devised to somewhat alleviate the pressure fluctuations, more rational strategies based on firm physical understanding are still highly desired.

Reference [39] noticed the remarkable similarity between the vortex rope in a draft tube and vortex breakdown on a delta wing (Fig. 20), and clarified the underlying physics for the first time. By tracing the axial development of the mean flow's local absolute instability/convective instability (AI/CI) behavior[6] along the draft-tube inlet cone, these authors found:

— under part-load condition, the swirling flow at the Francis turbine's draft tube inlet is absolutely unstable and dominated by helical modes, which leads to spiral vortex ropes (Fig. 20a) and severe pressure fluctuation;

— under higher part-load condition, the swirling flow is also absolutely unstable but dominated by axisymmetric mode, leading to a bubble-type vortex rope (Fig. 20b) with small-amplitude pressure fluctuation; and

— under full-load condition, the flow has only a very weak swirl and is convectively unstable with almost no pressure fluctuation.

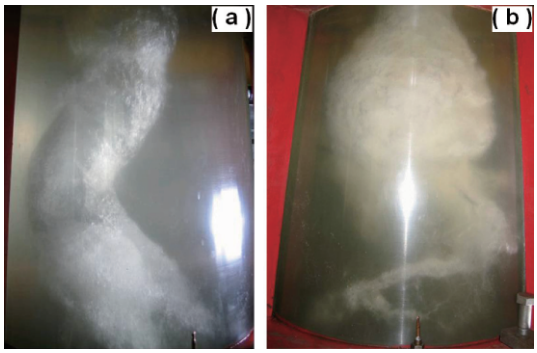

Figure 20: The spiral and bubble types of the vortex breakdown in a model draft tube.

Reference [41] has further identified that the absolute instability of the draft-tube flow was caused crucially by the reversed axial flow at the draft-tube inlet under part-load conditions. Thus, suppressing the reversed axial flow should be the key to reduce severe pressure fluctuations. They illustrated how this strategy could work by a numerical simulation of water injection at the draft-tube inlet. One result is shown in Fig.21, indicating that a jet with mass flux 10.2% of the draft-tube flow can effectively eliminate the pressure fluctuations.

External injection, however, needs extra power consumption and may not be practically feasible. Because the draft-tube inlet is the runner exit, a more radical strategy should be to redesign the runner blades so that the normal operating envelope can be maximally enlarged and reversed flow phenomenon be minimized. In other words, suppressing pressure fluctuation can be made in consistency with enhancing turbine's key performance (efficiency). This concept has been confirmed by [42] based on the axial component of (38) which he re-derived and is equivalent to (40).[7] Reference [42]

[6] For relevant knowledge of vortex instability and breakdown see, e.g. [40] and [7].

[7] The rotating runner surface has a centrifugal acceleration that

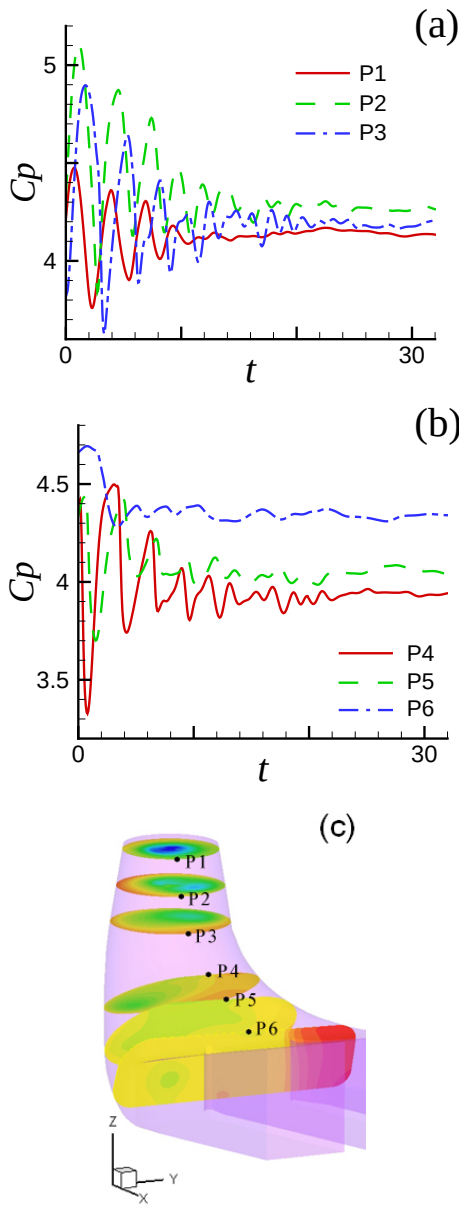

Figure 21: Pressure fluctuations on draft-tube wall under water-injection control: (a) and (b) are the pressure fluctuations on six check points, respectively; (c) shows the check points' locations [41].

used this formula as the objective function in his optimization procedure. As a result, since the optimized runner enhances the mean velocity at its exit, the reversed flow is considerably alleviated, and hence the pressure-fluctuation amplitude is remarkably reduced by 60%. The rotor blades geometry and runner efficiency before and after optimization are compared in Figs. 22(a) and (b), with the peak efficiency being increased from 93.6% to 94.5%.

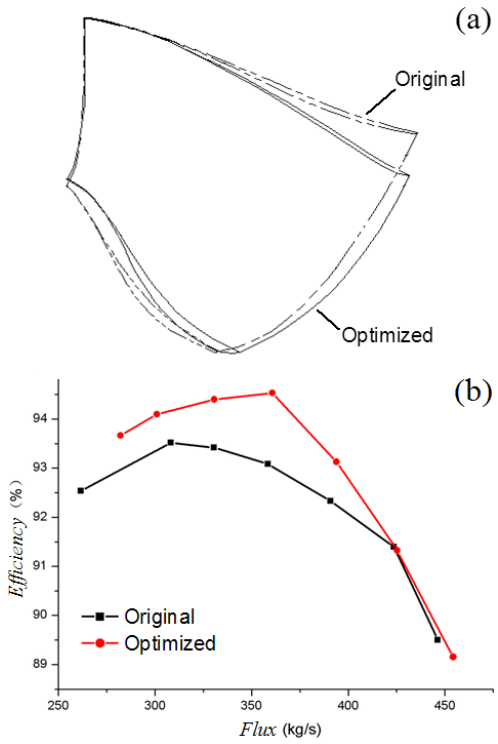

Figure 22: Comparison of (a) the runner blade shapes and (b) efficiencies of a Francis turbine before and after optimal design of the runner [42].

6 Concluding Remarks

1. The complexity of real flows at large Reynolds numbers lies at the coexistence and coupling of multiple fundamental processes in fluid dynamics and irreversible thermodynamics. Each process is measured by one or a few characteristic variable, of which the governing equation is nonlinear. The coupling of different processes occurs both in the interior of the flow field and on boundaries. The Helmholtz decomposition and its modern extension/sharpening permits examining separately the special feature and dominant structures of every process and its coupling with others, which forms a very useful theoretical framework in complex flow diagnosis. The more complex is the flow, the more strongly it is desired to decompose the flow field to the most elementary building block, and hence the more one would need to rely on such a theory. This basic idea is demonstrated in this article by considering the vorticity dynamics in complex flow diagnosis and management.

causes a $\boldsymbol{\sigma}_a$, which however has no contribution to axial moment, namely the surface integral of $x^2\sigma_{az}$ always vanishes.

2. It is proposed that, in the interior of a vortical flow the best flow-structure indicator is the Lamb vector $\boldsymbol{l} = \boldsymbol{\omega} \times \boldsymbol{u}$ along with its curl and divergence; while at the flow boundary the best process indicator is the pressure-caused boundary vorticity flux $\boldsymbol{\sigma}_p$ along with the boundary vorticity $\boldsymbol{\omega}_b$ or the on-wall shear stress $\boldsymbol{\tau} = \mu\boldsymbol{\omega}_b \times \boldsymbol{n}$.

3. The derivative-moment transformation (DMT) is one of the effective approaches to exhibit explicitly the role of local flow structures in global flow performance. A series of DMT-based total force/moment formulas are given as illustration, which permit pinpointing various key vortical structures and local processes by identifying the Lamb vector and the pressure-caused BVF in relevant integrands, ranging from axial vortices to near-wall free shear layers, boundary-layer separation, boundary layers, and eventually the vorticity creation from the wall. The identification of key indicators of local flow structures and processes, as well as their appearance in global flow performance leads to a local-dynamics flow diagnosis theory.

4. While examples from different application fields are given to illustrate the ability of local dynamics theory in the diagnoses and managements of complex external and internal flows, the theory and applications are still in continuous progress. New useful structure-interaction indicators or new aspects of our proposed indicators could be identified, and their roles in various classes of global performances could be further quantified. In particular, much more has to be done for high-speed complex flow diagnosis and management, which should be a major field of future exploration. The development at fundamental level and applications in engineering practice have to be mutually motivated.

Acknowledgement

The authors appreciate the valuable discussions with Profs. Yu-Lin Wu, Shu-Hong Liu, and Qiu-Shi Li on the applications of the local dynamics theory to turbo flows. We are also very grateful to Prof. Xie-Yuan Yin for his insightful comments on the early drafts of this article. Wu, Yang, and Zhang were supported in part by the Ministry of Science and Technology of China's Turbulence Program under Grant No. 2009CB724101, the National Basic Research Program of China under Grant No. 2007CB714600, and the Foundation for Innovative Research Groups of the National Natural Science Foundation of China under Grant No. 10921202. Lu was supported in part by the National Natural Science Foundation of China under Grant Nos. 11072236 and 10832010.

References

[1] Helmholtz, H., "Über integrale der hydrodynamischen gleichungen, welche den wirbelbewegungen ensprechen", *J. Reine Angew. Math.*, Vol. 55, pp. 25–55, 1858. English translation: "On intergal of the hydrodynamical equations which express vortex motion", *Phil. Mag.*, Vol. 34, pp. 15-24, 1867.

[2] Kelvin, Load, "On vortex motion", *Trans. R. Soc. Edinb.* Vol. 25, pp. 217-260.

[3] Lord Rayleigh, *"The Theory of Sound"*, Dover, 1929.

[4] Lagerstrom, P.A., Cole, J.D. and Trilling, L., "Problems in the theory of viscous compressible fluids", *Technical report*, California Institute of Technology, Pasadena, California, 1949.

[5] Kovasznay, L.S.G., "Turbulence in supersonic flow", *J. Aero. Sci.*, Vol. 20, pp.657–682, 1953.

[6] Chu, B.T. and Kovasznay, L.S.G., "Non-linear interactions in a viscous heat-conducting compressible gas", *J. Fluid Mech.*, Vol. 3, pp. 494–514, 1958.

[7] Wu, J.Z., Ma, H.Y. and Zhou, M.D., "*Vorticity and Vortex Dynamics*", Springer, 2006.

[8] Truesdell, C., "*The Kinematics of Vorticity*", Indiana University Press, Bloomington, IN, 1954.

[9] Mao, F., Shi, Y.P. and Wu, J.Z., "On a general theory for compressing process and aeroacoustics: linear analysis". *Acta Mech. Sinica*, Vol. 26, pp.355–364, 2010.

[10] Mao, F., Shi, Y.P. and Wu, J.Z., "A note on general theory for compressing process". Submitted for publication, 2010.

[11] Howe, M.S., "Contribution to the theory of aerodynamic sound with application to excess jet noise and the theory of the flute", *J. Fluids Mech.*, Vol. 71, pp. 625–673, 1975.

[12] Lighthill, M.J., "*Introduction of the boundary layer theory*", In "*Laminar Boundary Layers*", Rosenhead, L. ed., Oxford University Press, 1963.

[13] Zhao, H., Wu, J.Z., and Luo, J.S., "Turbulent drag reduction by traveling wave of flexible wall", *Fluid Dyn. Res.*, Vol. 34, pp. 175–198, 2004.

[14] Wu, C.J., Wang, L. and Wu, J.Z., "Suppression of the von Kármán vortex street behind a circular cylinder by a travelling wave generated by a flexible surface", *J. Fluid Mech.*, Vol. 574, pp. 365–391, 2007.

[15] Du, Y. and Karniadakis, G.E., "Suppressing wall turbulence by means of a transverse traveling wave", *Science*, Vol. 288, pp. 1230–1234, 2000.

[16] Du, Y., Symeonidis, V. and Karniadakis, G.E., "Drag reduction in wall-bounded turbulence via a transverse travelling wave", *J. Fluid Mech.*, Vol. 457, pp. 1–34, 2002.

[17] Prandtl, L. "Tragflügeltheorie, I.: Mitteilungen", *Nachrichten Ges. Wiss. Götingen, Math-Phys. Kl.*, pp. 151–177, 1918.

[18] von Kármán, T. and Burgers, J.M., "*General aerodynamic theory – perfect fluids*", In Durand, W.F. ed., "*Aerodynamic Theory*", Vol. II, Springer, 1935; Dover, 1963.

[19] Lighthill, M. J. "Physical interpretation of the mathematical theory of wave generation by wind", *J. Fluid Mech.*, Vol. 14, pp. 385–398, 1962.

[20] Saffman, P.G., "*Vortex Dynamics*", Cambridge University Press, 1992.

[21] Yang, Y.T., Su, W.D. and Wu, J.Z., "Helical wave decomposition and applications to channel turbulence with streamwise rotation", *J. Fluid Mech.*, In press, 2010.

[22] Tong, B.G., Yin, X.Y. and Zhu, K.Q., "*Theory of Vortex Motion*", 2nd Ed., The University of Science and Technology of China Press, 2009. In Chinese.

[23] Hamman, C.W., Klewicki, J.C. and Kirby, R.M., "On the Lamb vector divergence in Navier-Stokes flows", *J. Fluid Mech.*, Vol. 610, pp. 261–284, 2008.

[24] Chen, L.W., Xu, C.Y. and Lu, X.Y., "Numerical investigation of the compressible flow past an aerofoil", *J. Fluid Mech.*, Vol. 643, pp. 97–126, 2010.

[25] Wu, J.Z., Wu, H. and Li, Q.S., "Boundary vorticity flux and engineering flow management", *Adv. Appl. Math. Mech.*, Vol. 1, pp. 353–366, 2009.

[26] Li, Q.S., Wu, H., Guo, M. and Wu, J.Z., "Vorticity dynamics in axial compressor flow diagnosis and design - part II: Methodology and application of boundary vorticity flux", *J. Fluids Eng.*, Vol. 132, No.011102, 2010.

[27] Yang, Y.T., Zhang, R.K., An, Y.R. and Wu, J.Z., "Steady vortex force theory and slender-wing flow diagnosis", *Acta Mech. Sinica*, Vol. 23, pp. 609–619, 2007.

[28] Smith, F.T., "On the high reynolds number theory of laminar flows", *IMA J. Appl. Math.*, Vol. 28, Number 3, pp. 207–281, 1982.

[29] Wu, J.Z., Lu, X.Y. and Zhuang, L.X., "Integral force acting on a body due to local flow structures". *J. Fluid Mech.*, Vol. 576, pp. 265–286, 2007.

[30] Wu, J.C., "*Elements of Vorticity Aerodynamics*". Tsinghua University Press, Beijing, China, 2005.

[31] Burgers, J.M., "On the resistance of fluids and vortex motion". *Koninklijke Nederlandsche Akademie van Wetenschappen Proceedings*, Vol. 23, Number 1, pp. 774–782, 1921.

[32] Wu, J.C., "Theory for aerodynamic force and moment in viscous flows". *AIAA J.*, Vol. 19, pp. 432–441, 1981.

[33] Lighthill, M.J., "Fundamentals concerning wave loading on offshore structures." *J. Fluid Mech.*, Vol. 173, pp. 667–681, 1986.

[34] Sun, M. & Wu, J. H., "Large aerodynamic force generation in a sweeping wing at low Reynolds numbers." *Acta Mech. Sinica*, Vol. 20, pp. 24-31.

[35] Xu, C.Y., Chen, L.W. and Lu, X.Y., "Large-eddy simulation of the compressible flow past a wavy cylinder". *J. Fluid Mech.*, 2010. Accepted.

[36] Zhang, R.K., "Diagnosis, optimization and control in complex flows based on local-dynamics theory". Ph.D. dissertation, Peking University, Beijing, China, 2010. In Chinese.

[37] Yang, Y.T., Wu, H., Li, Q.S., Zhou, S. and Wu, J.Z., "Vorticity dynamics in axial compressor flow diagnosis and design", *J. Fluids Eng.*, Vol. 130, No.041102, 2008.

[38] Li, Q.S. and Guo, M., "Diagnosis and design of a low speed compressor based on local dynamics", *Adcances in Natural Science*, Vol. 15, Number 2, pp. 221–228, 2005. In Chinese.

[39] Zhang, R.K., Cai, Q.D. and Wu, J.Z., "The physical origin of severe low-frequency pressure fluctuations in giant Francis turbines", *Modern Physics Letters B*, Vol. 19, Number 28&29, pp. 1527–1530, 2005.

[40] Yin, X.Y. and Sun, D.J., "*Vortex Stability*", National Defence Industrial Press, Beijing, China, 2003. In Chinese.

[41] Zhang, R.K., Mao, F., Wu, J.Z., Chen, S.Y., Wu, Y.L. and Liu, S.H., "Characteristics and control of the draf-tube flow in part-load Francis turbine", *J. Fluids Eng.*, Vol. 131, No.021101, 2009.

[42] Wu, X.J., "The numerical simulation of the usteady flow of the Fransic turbine and vortical flow diagnosis", Ph.D. dissertation, Tsinghua University, Beijing, China, 2009. In Chinese.